Nano-device Fabrication from Quantum Dot Assembly

by

Wei Su

A dissertation submitted to the Graduate Faculty in Chemistry in partial fulfillment of the requirements for the degree of Doctor of Philosophy, The City University of New York

2012

This manuscript has been read and accepted for the Graduate Faculty in Chemisty in satisfaction of the dissertation requirement for the degree of Doctor of Philosophy.

Prof. Hiroshi Matsui, Hunter College

[**required signature**]

Date

Chair of Examining Committee

Prof. Maria Tamargo

[**required signature]**

Date

Executive Officer

Prof. Charles M. Drain

Prof. Vinod M. Menon

Supervisory Committee

THE CITY UNIVERSITY OF NEW YORK

Abstract

Nano-device Fabrication from Quantum Dot Assembly

by

Wei Su

Adviser: Professor Hiroshi Matsui

Colloidal semiconductor nanocrystals are highly photoluminescent crystalline nanoparticles (also termed as: quantum dots, QDs) with diameters ranging typically from 1 to 10 nm. For over a decade, quantum dots have been applied in various areas ranging from biological imaging, novel sensors to electroluminescence light-emitting diode (LED) due to their unique optical and electrical properties, such as broad excitation region, tunable size-dependant photoluminescence, high quantum yield, excellent chemical stability as compared to conventional organic dyes, and narrow emission peaks.

We successfully designed and built two fluorescence resonant energy transfer (FRET) donor-acceptor assemblies between quantum dots. Each assembly was characterized by steady-state and time-resolved photoluminescence measurements at different donor-to-acceptor ratios. Both photoluminescence quenching and decrease in the lifetime of donor quantum dots provided a concrete evidence of occurrence of FRET in each quantum dots pair assembly. Accompanied by the tunability of the emission energy of quantum dots in the broad visible region, our investigations on QD-QD FRET pairs present an attractive approach towards developing efficient light emitters and bio-sensors. Furthermore, we explored to build a novel microcavity by embedding one QD-QD between two distributed Bragg reflectors (DBRs). The spontaneous emission of QDs embedded inside a quasi one-dimensional microcavity should be further enhanced by FRET from the donor QD to the acceptor of QD.

Bio-templating is a promising alternative method for semiconductor nanowire synthesis since it offers a variety of advantages such as low energy consumption for the synthesis and eases of template bionanotube preparation and CdS coating process. As a continued work, we exploited the direct nucleation and growth of CdS nanocrystals on the biomolecular nanowires without using the mineralization peptides. The whole synthesis process is completed in simple two steps without the uses of catalytic peptides or capping agents, commonly used for various nanoparticle synthesis. We also report a peptide molecule that self-assembles at the air-water interface and is capable of reducing gold ions and coordinating them to form triangular nanoplatelets and related structures. We show that we are able to control both morphology and crystallinity of gold nanoplatelets as a function of surface pressure.

This is

dedicated to

My wife: Li Fan

My son: Leonardo Su

Acknowledgements

First and foremost, I would like to give my wholehearted gratitude to my dear mentor, Professor Hiroshi Matsui, for his inspiring guidance, unconditional devotion, and enlightening instructions in the joyful but challenging journey of my PhD study.

I also own thanks to my research committee members, Prof. Michael Drain, Prof. Vinod Menon. This dissertation cannot be so fruitful without their continuous guidance and advice.

As a research collaborator, I own special thanks to Prof. Raymond Tu and Dr. Lorraine Leon, Mr. Harish Natarajan and Ms. Catherine Callo. Our collaborating has been enjoyable and fruitful.

I own thanks to my previous colleagues in our lab: Dr. Christophe Pejoux, Dr. Hanying Bai, Dr. Xueyun Gao, Dr. Roberto de la Rica, Dr. Nurxat Nuraje, Dr. Linglu Yang, Dr. Anita Swami, Dr. Jungsun Lim, Dr. Fen Xu and current colleagues: Dr. Yoshiyaki Maeda, Ms. Luona Anjia, Ms. Prerna Kaur, Ms. Kristina Fabijanic, Ms. Menglu Shi, Mr. Zengyan Wei and Ms. Parminder Jeet Kaur. I own thanks to friends from other labs: Dr. Jorge Marolas, Dr. Areti Tsiola, Dr. Zheng Liu, Mr. Xiaoze Liu and Mr. David Goldberg.

Most of all, I own thanks to my dear parents: Ms. Huanping Liu and Mr.Yingqing Su, my brother: Mr. Lei Su, parents-in-law: Mr. Xiangming Fan and Ms. Xiaoying Wu.

Finally, I want to express my gratitude to my wife: Ms. Li Fan and my son: Leonardo Su.

I also gratefully acknowledge the financial supports from DOE and NIH.

Wei Su

Table of Contents

List of Figures

List of Schemes

Chapter 1. Fluorescence Resonant Energy Transfer (FRET) between Type I CdSe-ZnS and type II CdS-ZnSe Quantum Dots Assemblies

1.1 Introduction

For over a decade, QDs have found applications in various areas ranging from biological imaging,[1, 2] novel sensors to electroluminescence light-emitting diode (LED) due to their unique optical and electrical properties.[3, 4] QDs have broad absorption band, size-dependant photoluminescence (PL) property, high quantum yield (QY), and excellent chemical stability as compared to conventional organic dyes[5] in addition to narrow emission peaks. Among QDs, type II core-shell QDs such as CdS-ZnSe, ZnO-CdS and CdSe-CdTe received significant attention due to their unique band alignment where the band structures of the core and the shell materials are staggered and one carrier is predominantly confined to the core and the other is located in the shell with photon excitation.[6, 7] This feature contrasts to the commonly studied type I QDs where both carriers are confined in the same physical domain for type I QD scenario.[8] For the type II QDs, the recombination rate between the electron and the hole is diminished due to the reduced wavefunction overlap between the carriers and thus has longer exciton lifetime.

Förster resonance energy transfer (FRET) is a non-radiative energy transfer mechanism between an excited donor fluorophore and a ground-state acceptor fluorophore through dipole-dipole interactions.[9] Three important requirements have been reported for the necessary conditions of FRET between donors and acceptors: (i) The photon emission energy of donors has to be greater than that of acceptors,[10] (ii) The donor emission band and the acceptor absorption spectra has sufficient overlap, and (iii) The distance between donors and acceptors is within the distance limit of FRET (~10 nm).[11] If all three requirements are met, the resonance energy transfer between donors and acceptors occurs in high probability and the FRET induces both PL intensity quenching and reduction of the carrier lifetime of the donor.[10]

QDs were examined as donors in FRET-based studies to replace traditional fluorescent dyes in biological applications such as biological imaging, [12] DNA detection, [13] and cell tracking.[14] The FRET-based sensor is a great example to take advantage of QDs as donors because the narrow emission band of QD donors does not interfere with the direct excitation of acceptors and thus detect only signals induced by FRET. This is extremely important in the design of such bio-sensors since the emission band of acceptor enhanced by FRET could be detected easily from large background PL bands. From the PL intensity change of acceptor in a bio-sensor system, one is able to examine the concentration of target biological molecules via antigen-antibody conjugation method. Driven by these important applications, the FRET mechanism between QDs and dye-labeled bio-molecules has been investigated in a variety of conditions (e.g. solvent, temperature, pH conditions, etc.).[5] However, few studies have been reported on the FRET with type II QDs. The use of type II QD as a donor is considered to be disadvantageous in the FRET system due to the fast electron-hole recombination before FRET occurs. Another potential drawback is that quantum yields (QYs) of type II QDs are lower than QYs of type I QDs due to the complete spatial separation of carriers in type II QDs.[15, 16, 17]

In this work we successfully assembled two set of QD-QD hybrid structures from type I CdSe-ZnS QDs and type II CdS-ZnSe QDs to study their energy transfer mechanisms through time-resolved and steady-state photoluminescence (PL) measurements. The type II QDs are expected to be excellent donors since the long excitonic lifetime of the donors enhances the probability for the energy transfer to the acceptor before electrons and holes of the donor recombine. Despite this potential, there has no report so far to explore type II QD as a donor in the FRET process. Another aim of this report is to investigate the comparison of the type II QDs as a donor and an acceptor in the QD-QD FRET complexes. These measurements reveal reduction of the donor lifetime, indicating the occurrence of FRET between type I and type II QD pairs in both cases, and the degree of the donor lifetime reduction is observed to be larger when type II QDs are used as donors. Experimental data supports that the long-range resonance-energy transfer is sufficiently effective between QDs and the enhancement is larger as the exciton lifetime of donors is extended, as expected by Förster theory.

1.2 Experimental Section

The type I CdSe-ZnS (QD491, QD626) and the type II CdS-ZnSe (QD560) QDs reported here were prepared by using a stepwise procedure composing of; 1) core nano-crystals growth (CdSe, CdS), 2) shell over-coating (ZnS, ZnSe), 3) tri-n-octylphosphine oxide (TOPO)/ tri-n-octylphosphine (TOP) -capping, and 4) size selection precipitation and final purification. [6, 18, 19, 20] The diameter of QD cores and the shell thickness were necessary to be precisely controlled in the synthesis in order to optimize the spectral overlap between the emission bands of the donors and the absorption bands of the acceptors.

1.2.1 Synthesis of CdSe-ZnS type I QD (QD491, QD626)

1.2.1.1 Synthesis of CdSe cores

First, 51.4 mg (0.4 mmol) of CdO (Aldrich) was placed into a flask containing 1.15 mL (1.045g) of Trioctylphosphane oxide (TOPO, 99%; Aldrich) and then it was mixed with 2.85 mL (2.375g) of hexadecylamine (HDA, 98%; Aldrich) at 270 °C under nitrogen flow. After 230 μL (0.8 mmol) of dodecylphosphonic acid was added and temperature of the resulting colorless solution was raised to 250 °C, 3.5 mL of a 0.2 M solution of Se (Aldrich) powder in trioctylphosphane (TOP) (97%; Aldrich) was quickly injected. The reaction was stopped after 45 seconds (for QD491) or 60 minutes (for QD626) by pouring the mixture into 30mL methanol (Aldrich) at room temperature. After the CdSe cores were purified by rinsing in methanol and centrifugation (14,000 RPM, 15 minutes), the resulting compounds were re-dispersed in hexane (Aldrich).

1.2.1.2 Coating ZnS shell onto CdSe cores

First, 14 g Trioctylphosphane oxide (TOPO) (99%; Aldrich), 3 mL oleylamine (99%; Aldrich), 2 mL HDA (98%; Aldrich), and 2.0 mmol bis(2,4,4-trimethylpentyl)phosphinic acid (BTMPPA, 99%; Aldrich) were degassed under vacuum for 2 hrs in a three-necked flask at 100°C. CdSe cores dispersed in hexane from previous synthesis were added to the degassed solution and the hexane was removed at 80°C under vacuum. Under a flow of argon, the mixed solution was heated at 180°C and the ZnS shell precursor solution

(0.1mmol diethylzinc (95%; Aldrich) and 0.1mmol hexamethyldisilthiane (>97%; Fluka) dissolved in 7 mL TOP) was added dropwise. After the addition was complete, the solution was kept at 180°C for 5 min and then left stirring overnight at 75°C to anneal the ZnS shell. The resulting CdSe-ZnS core-shell QDs were purified by precipitation in methanol, same as the core-purification procedure. The final QDs were re-dispersed in hexane.

1.2.2 Synthesis of CdS/ZnSe type II QDs (QD560)

1.2.2.1 Synthesis of CdS cores

The Cd precursor solution was prepared by mixing a degassed (under vacuum at 100°C for 1 h) solution of cadmium acetate hydrate (1 mmol), trioctylphosphane (TOP) (6 mL), and bis(2,4,4-trimethylpentyl)phosphinic acid (BTMPPA) (1 mmol) with a degassed (under vacuum at room temperature for 1 h) solution of elemental sulfur (1 mmol, Aldrich) in oleylamine (3 mL, Aldrich). The resulting solution was rapidly injected into a round-bottomed flask containing degassed (under vacuum at 100°C for 1 h) oleylamine (7 mL, 98%) and trioctylphosphane (TOP) (8 mL) stirring rapidly at 250–280°C. After QDs were grown at 250°C for 15 to 30 min, the heating was stopped and cooled down by removing the heating source. Before coating the ZnS shell, the CdS QD cores were precipitated out of the growth solution and then separated from hexane solution one more time to remove unreacted precursors and excess capping ligands. The resulting particles were flocculated from the growth solution by adding 0.4 equiv of hexane, 0.8 equiv of butanol, and 3 equiv of methanol (total 100mL) to 1 equiv of growth solution (24mL) and centrifuged for 15 min at 14,000 RPM. These particles were dispersed in hexane and flocculated by adding one drop of butanol per equivalent of original growth solution and 0.5 equiv of methanol, and then centrifuged for 15 min. The CdS core nanoparticles were finally re-dispersed in pure hexane.

1.2.2.2 Coating of ZnSe shell onto CdS cores

A colloidal solution of ca. 20 mg of CdS QD cores was placed in a three-neck flask under purified argon flow. After adding 2.5 mL of TOPO with 1.5 mL of HDA, the mixture was heated at 190 °C and then kept at this temperature to evaporate hexane completely. Zinc stearate (316 mg, 98%; Aldrich) was dissolved in 2.5 mL of toluene upon gentle heating (ca. 60 °C). After cooling to room temperature, the resulting 0.2 M solution was mixed with 2.5 mL of a 0.2 M solution of Se in TOP. This mixture was injected with a syringe pump within 1 hr into the reaction flask containing the CdS core nanocrystals at 190 °C. Periodically small aliquots were removed in order to monitor the shell growth by TEM. After the addition was completed, the resulting crystals were annealed at 190 °C for additional 1-1.5 hrs. The core-shell QDs were purified by the precipitation method same as the core-processing procedure. The final CdS-ZnSe type II QDs were re-dispersed in hexane.

The small (QD491) and large (QD626) CdSe-ZnS type I QDs consist of CdSe cores with diameters of 3.9±0.1 and 5.5±0.1 nm, determined by transmission electron microscopy (TEM). Both CdSe cores were over-coated by ZnS shell with a thickness of ~1 nm. The CdS-ZnSe (QD560) type II QDs consist of CdS core with a diameter of 4.0±0.3 nm and the ZnSe shell with a thickness of ~1 nm. For all QDs in this report, TOPO and TOP were used as ligands to passivate surfaces of core-shell QDs.

All QD samples were casted by spin coating solution of QDs in hexane onto a 1.0cm x 1.0cm silicon substrate under ambient atmosphere. Following the spin coating, the samples were placed in an oven at 40 ˚C for 1 hour to remove the trace amounts of organic solvents, before they were characterized by steady-state PL and time-resolved PL.

The control samples for the type II QD560-type I QD626 assembly consist of either only the donor of CdS-ZnSe (QD560) or the acceptor of (QD626) CdSe-ZnS QDs. Similarly, the control samples for the type I QD491-type II QD560 assembly consist of either only the donor of (QD491) CdSe-ZnS QDs or the acceptor of CdS-ZnSe (QD560) QDs. All control samples were prepared exactly the same concentration as the one in the corresponding mixed QD samples on silicon. The donor-to-acceptor stoichiometry ratio was varied in the mixed QD samples by keeping the concentration of donor QDs constant and varying the concentration of acceptor QDs.

The steady-state fluorescence spectra were acquired using a spectrometer (Horiba Jobin-Yvon) with a Xenon lamp as an excitation source at 367 nm. The time-resolved fluorescence measurements were carried out using a time-correlated single photon counting (TCSPC) system (Horiba Jobin-Yvon) at room temperature. A 200 ps diode laser operating at 1 MHz repetition rate and 467 nm emission wavelength was used as the excitation source. The time-resolved data were deconvoluted by using the iterative nonlinear least squares method. Absorption spectra were recorded by a Cary 50 Probe UV-vis spectrophotometer in the wavelength range of 400-700 nm. Transmission Electron Microscopy (TEM) samples were prepared by attaching a carbon-coated copper TEM grid on a piece of 1.0cm x 1.0cm silicon substrate, applying spin-coating procedure to the same volume of QD solution, then peeling the TEM grid off from the silicon substrate after baking it for 1 hour at 40 ˚C. All TEM samples were studied by Zeiss EM 920 Transmission Electron Microscope at an acceleration voltage of 80 kV.

Two sets of FRET-based QD assemblies (the assembly of type II QD560 donor- type I QD626 acceptor and the assembly of type I QD491 donor- type II QD560 acceptor) with different donor-to-acceptor stoichiometry ratios were prepared and studied by using steady-state and time-resolved PL spectroscopy. The concentration of QD solution was determined analytically from the total amount of Cd and the sizes of QDs. For example, for the QD491, the CdSe core was dried and weighed as 16.24mg after synthesis. The number of CdSe QD core is about 9.0×10^{16} assuming each CdSe QD weighs 1.8×10^{-19}g estimated from the diameter of 1.95nm and the density of 5.816g/cm^{3}. After the CdSe core was coated by ZnS and finally redispered in 200mL of hexane, the concentration of QD491 solution is 7.5×10^{-7} M.

In the first set of the QD560-QD626 QD assembly, to fix the donor-to-acceptor molar ratio as 2:1, the concentration of both CdS-ZnSe (QD560) and CdSe-ZnS (QD626) were kept constant as $4.5\text{x}10^{14}$ cm^{-3} ($7.5\text{x}10^{-7}$ M) and $2.25\text{x}10^{14}$ cm^{-3} ($3.75\text{x}10^{-7}$ M), respectively. For the second assembly of QD491-QD560 QDs, the donor-to-acceptor molar ratio of CdSe-ZnS (QD491) QDs and CdS-ZnSe (QD560) QDs was varied among 10:1, 5:1 and 2:1 while the concentration of CdS-ZnSe (QD560) QD was varied among $3.6\text{x}10^{13}$ cm^{-3} ($6.0\text{x}10^{-8}$ M), $7.2\text{x}10^{13}$ cm^{-3} ($1.2\text{x}10^{-7}$ M) and $1.8\text{x}10^{14}$ cm^{-3} ($3.0\text{x}10^{-7}$ M) and the concentration of CdSe-ZnS (QD491) QD was maintained as constant of $3.6\text{x}10^{14}$ cm^{-3} ($6.0\text{x}10^{-7}$ M).

1.3 Results and Discussion

The band alignments of type II QD560 donor – type I QD626 acceptor and type I QD491 donor – type II QD560 acceptor assemblies are shown in Figs. 1.1

Figure 1.1 (a) The band alignment of first QD assembly CdS-ZnSe (QD560) type II donor and CdSe-ZnS(QD626) type I acceptor quantum dots. (b) The band alignment of second QD assembly CdSe-ZnS (QD491) type I donor and CdS-ZnSe (QD560) type II acceptor quantum dots.

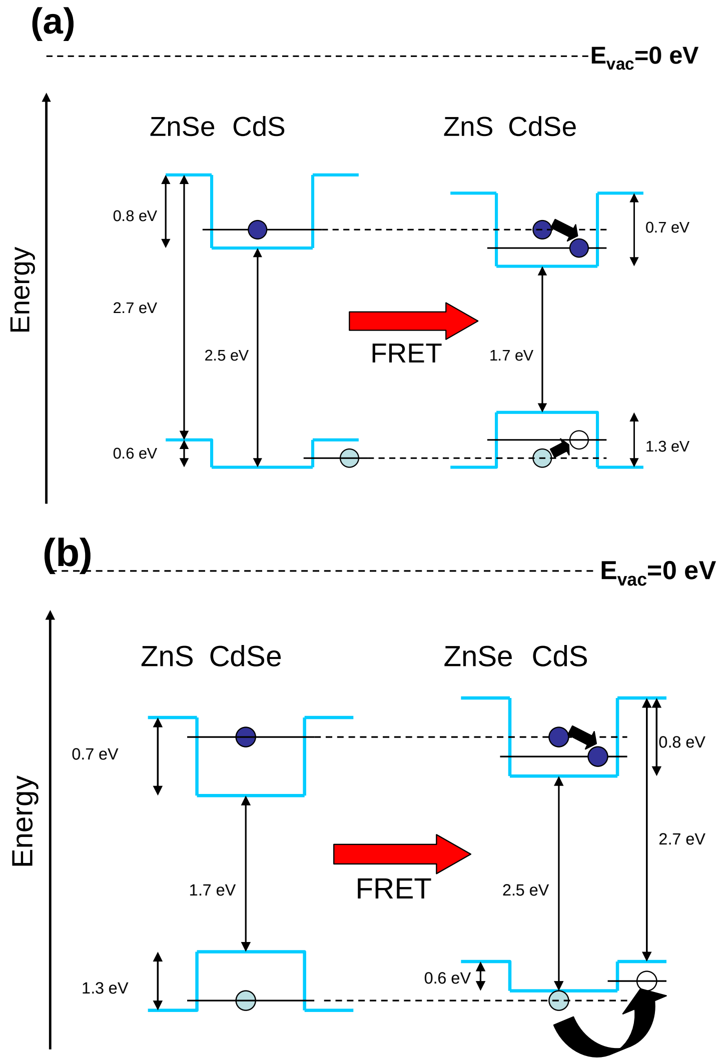

For the first assembly (Fig. 1.1-a), when the energy is transferred from type II CdS-ZnSe (QD560) QDs to type I CdSe-ZnS (QD626) QDs, the excited electrons and holes in the type I QD acceptor relax to the corresponding ground state by emitting photons. For the second assembly (Fig. 1.1-b), as the energy is transferred from type I CdSe-ZnS (QD491) QDs to the core of type II CdS-ZnSe (QD560) QDs, the excited electrons and holes relax to the ground state of the conduction band in CdS and the valence band in ZnSe, respectively, according to the type II band alignment, resulting in the type II emission.

Figs. 1.2 -a, -b indicate that there is sufficient overlap between the PL emission of type II QD560 and the lowest-energy absorption band of type I QD626 for the first QD assembly in Fig. 1.1-a for the FRET transition. The spectral overlap between the PL emission of type I QD491 and the lowest-energy absorption band of type II QD560 for the second QD assembly is also sufficient for the FRET as shown in Fig. 1.1-b. The small Stokes shift of the PL emission of acceptor QDs with respect to their lowest-energy absorption peaks indicates that these QDs had very few surface defects and have well-passivated surfaces. [6]

(a) FRET in the assembly of type II QD (donor) and type I QD (acceptor)

To investigate FRET of the first QD assembly between type II QD560 donor and type I QD626 acceptor in Fig. 1.1(a), we first monitored the changes in the PL intensity of both QD560 and QD626. Fig. 1.3 (a) shows normalized PL spectra of neat QD560 and QD626 QDs solid samples prepared in concentration of $4.5\text{x}10^{14}$ cm^{-3} ($7.5\text{x}10^{-7}$ M) and $2.25\text{x}10^{14}$ cm^{-3} ($3.75\text{x}10^{-7}$ M), respectively. When the type I-type II mixed solid sample was prepared using the same concentrations of neat QD solution, the PL spectrum of the mixed solid sample shows a double peak profile, deconvoluted to two Gaussian profiles (green lines) corresponding to the PL of neat QD560 and QD626 solid samples. In Fig. 1.3(a), the FL peak of donor QD560 is quenched and the peak of acceptor QD626 is enhanced with respect to the corresponding PL spectra of neat QDs.

Figure 1.2 (a) Steady state photoluminescence spectra of CdS-ZnSe (QD560) type II (black solid curve) and CdSe-ZnS(QD626) type I quantum dots (blue solid curve) and absorption spectra of CdSe-ZnS(QD626) (red solid curve). (b) Steady state photoluminescence spectra of CdSe-ZnS(QD491) type I quantum dots (black solid curve) and CdS-ZnSe (QD560) type II (blue solid curve) and absorption spectra of CdS-ZnSe (QD560) type II (red solid curve)

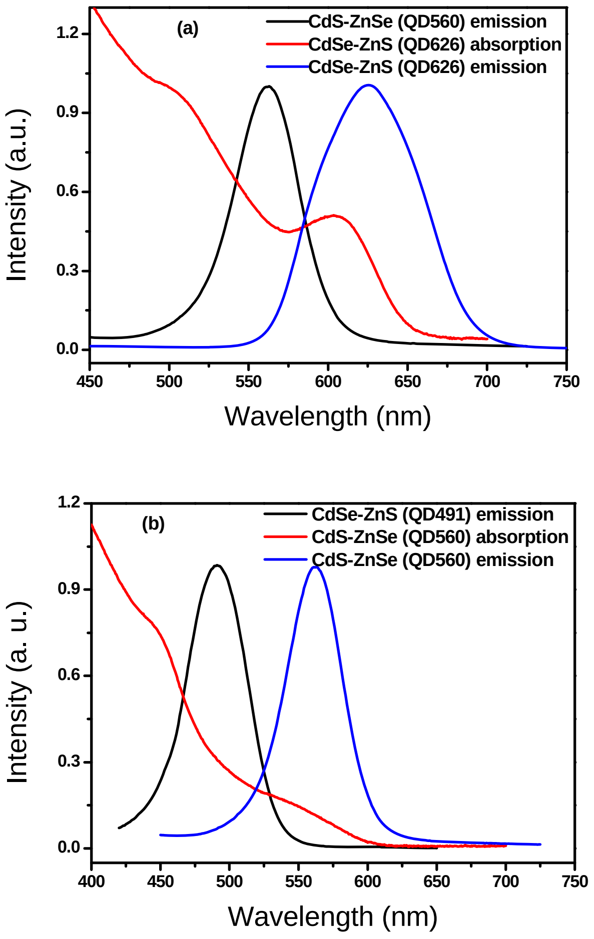

The efficiency of the quenching process via FRET in Fig. 1.3 (a) is quantified by using the Eq. (1): $Q=(I_{\mathrm{Free}}-I_{\mathrm{Mix.}})/I_{\mathrm{Free}}$, [21] where I_{Free} and $I_{\mathrm{Mix.}}$ are integrated intensities of neat QD560 PL band in the solid state sample and the intensity of the same band in binary QD assembly, the type II donor QD560 - type I acceptor QD626, respectively, under the same QD560 concentration. From this equation, PL intensity of the QD560 is effectively quenched by 74.1% in the mixed QD solid state sample with donor-to-acceptor ratio of 2:1. The efficiency of enhancement of PL emission of type I acceptor QD626 is calculated by Eq.(2): [16] $E=(I_{\mathrm{Mix.}}-I_{\mathrm{Free}})/I_{\mathrm{Free}}$, where I_{Mix}. and I_{Free} are integrated PL intensities of QD626 in the mixtures with QD560 and the PL intensity of the same band in theneat QD626 sample, respectively, under the same QD626 concentrations. In this case, the PL intensity of type I acceptor QD626 in the mixture QD sample is enhanced by 59.7% due to FRET from the donor QD560.

To further evaluate the FRET process between the type II donor QD560 QD and the type I acceptor QD626 QD, we carried out time-resolved PL measurement. The time-resolved PL spectra of neat QD560 QD solid sample and the mixed QD560-QD626 samples are shown in Fig. 1.3 (b) at the excitation wavelength 467 nm with the collection wavelength of 560±3nm. The PL lifetime of the type II donor QD560 decreases significantly from 8.33ns to 4.13ns in the presence of type I acceptor QD626. This result indicates that the quenching is caused by the energy transfer from QD560 to QD626 via the FRET process. The energy transfer efficiency from QD560 to QD626 is determine by Eq. (3) as below: [17]

$$\tau_{\mathrm{mix.}}{}^{-1}=\tau_{\mathrm{free}}{}^{-1}+\Gamma_{\mathrm{FRET}}$$

Figure 1.3 (a) Steady state photoluminescence spectra of neat QD560 solid sample (black solid curve), neat QD626 solid sample (blue solid curve), mixture of QD560-QD626 solid sample at ratio of 2:1 (red solid curve). The green solid lines are the results of Gaussian function fitted the photoluminescence of mixture QDs sample with two separate corresponding to the photoluminescence spectra of neat QD560 and QD626. (b) Time-resolved photoluminescence spectra (excited at 467nm wavelength) of neat QD560 QDs and in the QD560-QD626 mixed solid sample. The green solid lines are the fitting of each photoluminescence lifetime.

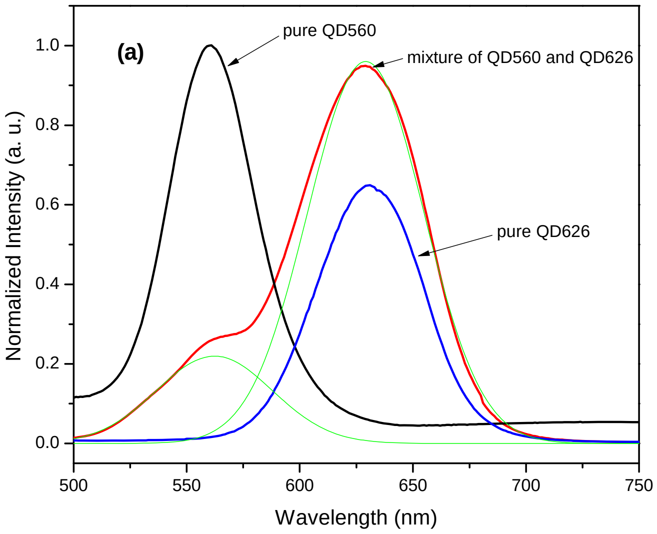

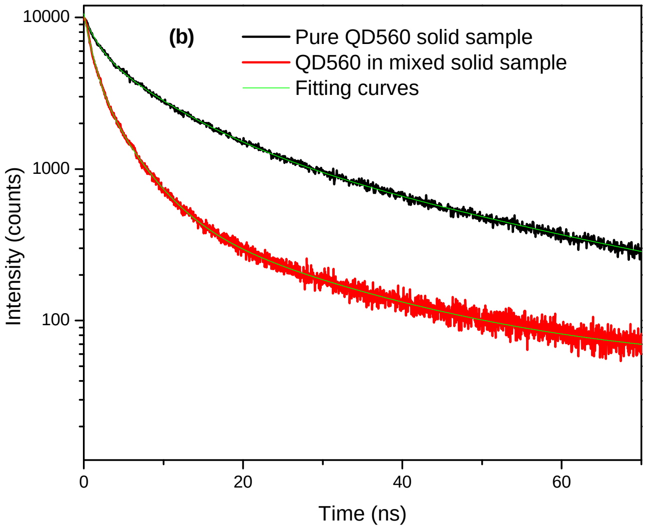

where τ_{mix} and τ_{free} are the lifetime of the donor in the presence and absence of acceptor, respectively, and the Γ_{FRET} is the energy transfer rate. Then energy transfer efficiency is calculated by Eq. (4) as following: [17]

$$E = \tau_{mix} \bullet \Gamma_{FRET}$$

The reduction of PL decay lifetime of the type II donor QD560 from 8.33 ns (in the absence of QD626) to 4.13 ns (in the presence of QD626) leads to the energy transfer efficiency as 50.4% in this QD assembly from the above equation. It should be noted that this energy transfer efficiency is comparable with the magnitude of energy transfer efficiency the in mixed QD system of CdSe/ZnS-CdSe/CdTe.[16]

(b) FRET in the assembly of type I QD (donor) and type II QD (acceptor)

The second QD assembly system, type I donor QD491 – type II acceptor QD560 (Fig. 1.1-b), was also examined to compared with the results in section 3-(a). A series of solid samples by varying the concentration of QD560 were studied with the fixed concentration of QD491 in the QD-QD FRET assembly. It is worth noting that the FRET was highly efficient in the first assembly of type II QD560- type I QD626 even in the 2:1 ratio. However, for the type I QD - type II QD assembly, the FRET is expected to be less discernable even at the same ratio because the decay time of donor is shorter than that of acceptor due to the fast electron-hole recombination of the type I QD donor. Hence three different mixed solid samples were prepared from CdSe-ZnS (QD491) QDs and CdS-ZnSe (QD560) QDs at the donor-to-acceptor molar ratios of 10:1, 5:1 and 2:1. To achieve this ratios, the concentration of CdS-ZnSe (QD560) QDs was adjusted among 3.6x10^{13} cm^{-3} (6.0x10^{-8} M), 7.2x10^{13} cm^{-3} (1.2x10^{-7} M) and 1.8x10^{14} cm^{-3} (3.0x10^{-7} M) and then they were mixed with CdSe-ZnS (QD491) QDs at the constant concentration of 3.6x10^{14} cm^{-3} (6.0x10^{-7} M). The Gaussian function-fitted spectra can be deconvoluted into neat QD491 and QD560 PL peaks for all of three mixed solid samples. The quenching of type I donor QD491 is observed in Fig. 1.4(a) as compared with the PL spectra of neat QD491 at the same concentration. PL intensity of QD491 is gradually decreased as the concentration of QD560 is increased in this type I donor QD - type II acceptor assembly.

Figure 1.4 (a) Quenching of the photoluminescence spectra of neat QD491 (black solid line), the mixtures of QD491-QD560 sample with ratio 10:1 (red solid line), 5:1 (blue solid line), 2:1 (green solid line). (b) Time-resolved photoluminescence spectra (excited at 467nm wavelength) of neat QD491 QDs and in the QD491-QD560 mixed solid sample with ratio 10:1 (red line), 5:1 (blue line), 2:1 (green line).

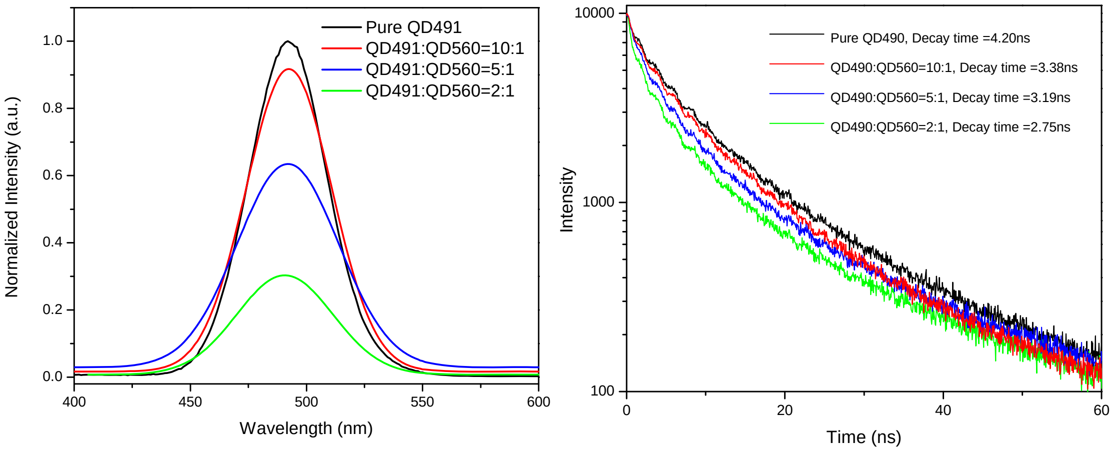

In order to calculate the quenching efficiency of the type I donor QD491 in the second QD assembly in Fig. 1.1-b, the same Eq. (1) $Q=(I_{\text{Free}}-I_{\text{Mix.}})/I_{\text{Free}}$, [21] is used, where I_{Free} and $I_{\text{Mix.}}$ are the integrated intensities of the neat QD491 PL band in the solid state sample and the intensity of the same PL band in the QD491-QD560 mixed solid sample, respectively, under the same QD491 concentration. From these spectra, the Q value is calculated to be 4.1%, 13.1% and 62.6%, for the donor-to-acceptor ratios of 10:1, 5:1 and 2:1. The increasing Q value shows its dependence on n (the number of acceptor QD560 per donor QD491), which indicates that the FRET efficiency is enhanced by increasing the number of the acceptor of QD560 around a donor of QD491.[23] This is because the number of acceptors per donor affects the FRET efficiency according to the following Eq. (5)

$$Eff=nR_0^6/(nR_0^6+r^6)$$

where $Eff.$ is FRET efficiency, n is the number of acceptors per donor, R_0 is Förster distance, and r is donor-acceptor distance. [5] Increasing n yields higher FRET efficiency when R_0 and r are fixed in this case.

Time-resolved PL measurements are also conducted to all mixed sample and neat QD491 sample for the binary QD assembly of the type I donor QD491 and the type II acceptor QD560 QD. The time-resolved PL spectra of these samples are shown in Fig. 1.4 (b). From the spectrum, the neat QD491 has a PL lifetime of 4.20ns. The PL lifetime decreases to 3.38ns, 3.19ns and finally reaches 2.75ns as the QD491-QD560 ratio is changed to 10:1, 5:1 and 2:1. This trend indicates that the quenching of type I donor QD491 is caused by FRET between QD491 and QD560 because the occurrence of FRET quenches PL lifetime of donors. [16] The energy transfer efficiency from QD491 to QD560 is determined by the same Eq. (3) as below: [17]

$$\tau_{mix.}^{-1}=\tau_{free}^{-1}+\Gamma_{FRET}$$

where τ_{mix} and τ_{free} are the lifetime of the QD491 in the mixed samples and the lifetime of the neat QDs, respectively. The energy transfer efficiency for each sample is estimated by Eq. (4) to be 5.78%, 7.55% and 12.56% as the QD491-QD560 ratios are changed among 10:1, 5:1 and 2:1, respectively. This trend is consistent with the change in Q values on the same series of samples.

At the donor-to-acceptor ratio of 2:1, the energy transfer efficiency of the binary QD assembly of the type II donor QD560 and the type I acceptor QD626 (Fig. 1.1-a) is 50.4% while the energy transfer efficiency of the binary QD assembly of the type I donor QD491 and the type II acceptor QD560 (Fig. 1.1-b) is much lower at the efficiency of 12.56%. When the type I QDs are excited both electrons and holes are confined in the cores. However, in the case of the type II QDs, one carrier is confined in the core while the other is confined in the shell. Because of the spatial separation of carriers in the type II QDs, the recombination of carriers requires longer time and thus the type II QDs have longer PL lifetime than the type I QDs. In the first QD assembly, the donor of the type II QD560 QD is still in the excited state when the energy transfer is initiated due to the longer lifetime of the type II donor QD. In the case of the second QD assembly, the donor of the type I QD491 relaxes faster than the acceptor of type II QD560 to recombine two carriers, and thus the type I donor QD491 is inefficient in the FRET process. This is why the type I QDs have not been employed as acceptors in FRET assemblies, and even less FRET studies were done using the type II QDs as acceptors.

To measure the inter-particle distance of type I and type II QDs in the QD assemblies, transmission electron microscopy (TEM) analysis of each QD assembly was conducted. In Fig. 1.5 (a) both QD560 and QD626 QDs in the mixed sample are close packed, forming a glassy solid on the TEM grid where each QD remains separated from its neighbors by the organic capping groups. The separation between adjacent QDs is about 4.9±0.3 nm in the solid samples for the first QD assembly and 4.5±0.2nm for the second QD assembly. Combining this result and the spectroscopic observation, it is evident that both QD560-QD626 separation distance (4.9±0.3 nm) and QD491-QD560 separation distance (4.5±0.2nm) are within the FRET distance in the solid state samples prepared by spinning coating. It should be noted that this distance is consistent with the FRET assembly of CdSe-ZnS and CdSe-ZnTe QDs with the interparticle distance of 6.3 nm. [16]

Figure 1.5 (a) TEM image of QD560-QD626 QD mixed sample with ratio of 2:1 shows an average diameter of QD560 is 6.0±0.3 and QD626 is 6.5±0.1 nm with separation distance of 4.9±0.3 nm. Scale bar=20nm. (b) TEM image of QD491-QD560 QD mixed sample with ratio of 2:1 shows an average diameter of QD491 is 4.9±0.1 nm, separation distance between QD491 and QD560 is4.5±0.2 nm. Scale bar=20nm.

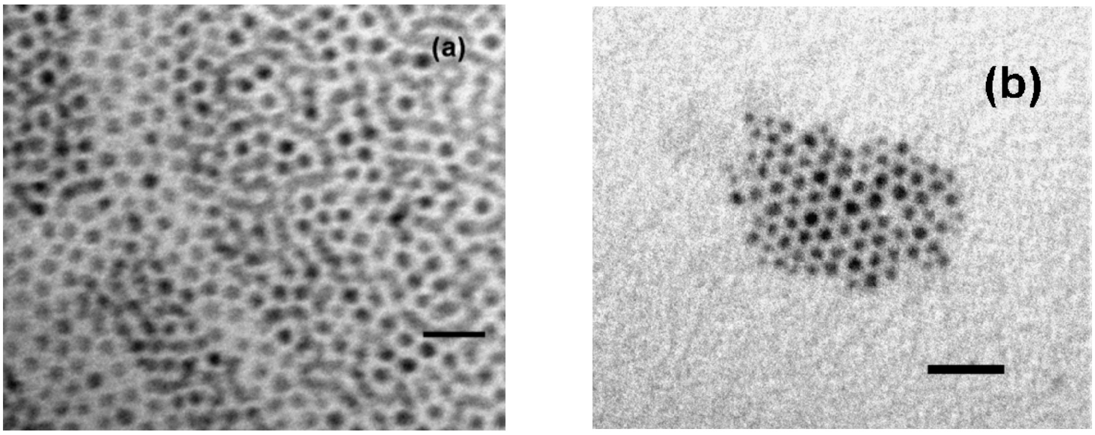

Sometimes the emission could be quenched by the aggregation of QDs, [23, 24] but this is not the case in our observation. If the aggregation of QDs is the main reason for the PL quenching, all of the QD samples in the second assembly should show the same quenching efficiency. However, both the PL and TRPL spectra clearly show that the quenching efficiencies are different among different donor-to-acceptor ratios. Especially for the QD491, the PL intensity is dramatically quenched (62.6%) in the presence of QD560 in the mixed sample, and the FRET efficiencies increase gradually as the percentage of QD560 is increased. Therefore, an aggregation of QDs is not the major pathway for the PL quenching in these experiments.

1.4 Conclusion

We have assembled solid state samples from the combinations of two QDs: 1) CdS-ZnSe (QD560) type II QDs (donor) and CdSe-ZnS (QD626) type I QDs (acceptor); 2) CdSe-ZnS (QD491) type I QDs (donor) and CdS-ZnSe (QD560) type II QDs (acceptor) with various mixing ratios. The FRET process between these donors and acceptors in the QD assemblies was confirmed by the PL intensity quenching and the decreased PL lifetime of donor QD in each assembly. The FRET efficiency of the type II donor -type I acceptor assembly is higher than the one for the type I donor - type II acceptor assembly even when both assemblies have the equal donor-to-acceptor ratio because of the difference in the excitonic lifetime of the donor QDs. The long lifetime of the donor QD increases the probability of the energy transfer to the acceptor QD before electrons and holes of the donor recombine yielding higher FRET efficiency in the type II – type I assembly.

Besides, it is worth highlighting that the energy gap between the donor QD and the acceptor QD on the basis of FL spectra, ~0.3 eV. is larger than their Stokes shift, ~0.05 eV, in the band gap diagram in Fig. 1.2. Since the emission bands of the donor and the acceptor are more separated, this feature was especially advantageous for the accurate measurements of FL lifetimes due to the elimination of the interference of donor emission spectra from the FRET-driven acceptor emission spectra.

Chapter 2. Biotemplating Fabrication of CdS Nanowires at Room Temperature

2.1 Introduction

CdS nanocrystals, II-VI semiconductor nanoparticles, have been extensively studied due to the unique optical and electrical properties including the broad excitation region, tunable size-dependant photoluminescence (PL), high quantum yield (QY), excellent chemical stability, and narrow emission peaks.[25, 26, 27] Recently, synthesis of one-dimensional CdS nanowires (NWs) has received much attention because of its potential application as building block for electronic and optoelectronic devices. There have reported two major approaches of synthesizing semiconductor NWs chemically: Vapor-liquid-solid (VLS) method and organic solution reaction of precursors in organic solvent at high temperature (over 200 ˚C). Both approaches have been well established, however these methods have some drawbacks as well. The VLS technique requires high reaction temperature (usually ~1000˚C) and the number of the species of VLS coatings are limited due to the availability of precursor vapors while the second method lacks the control of morphology in synthesized NWs. [28, 29]

Bio-templating is a promising alternative method for semiconductor NW synthesis since it offers a variety of advantages such as low energy consumption for the synthesis and eases of template bionanotube preparation and CdS coating process.[30, 31, 32] Furthermore, a large variety of well-defined bio-templates have been evolved to precisely control metal nanoparticle growth at the micro- or nano- level.[33, 34, 35] In order to synthesize CdS NWs that are applicable for building blocks of optoelectronic devices, high crystal quality and aspect ratio of the NWs are of great importance due to the critical requirement of the optical properties of the NWs and applications as electronic circuits, nanosensor arrays.[36, 37] Despites these advantages, the bio-templating synthesis of semiconductor NWs still needs to improve the yield and the quality of QDs by optimizing reaction steps and the growth speed to become effective for the practical applications.

Our previous works [38, 39, 40] have shown effective synthesis approaches in the growths of inorganic, semiconductor and metal NWs by employing biomolecular templates and specific mineralizing peptides on the template surfaces. Here, we exploited the direct nucleation and growth of CdS nanocrystals on the biomolecular nanowires without using the mineralization peptides. The bionanotubes provide coordinating groups (-COOH) to anchor Cd^{2+} and this site subsequently can react with S^{2-} for the completion of CdS growth on the bionanotubes. The whole synthesis process is completed in simple two steps without the uses of catalytic peptides or capping agents, commonly used for various nanoparticle synthesis. [41]

2.2 Experimental

2.2.1 Chemicals and regents

Analytic grade reagents of nonanedioic acid, 1-[3-(dimethylamino)propyl]-3-ethylcarbodiimide hydrochloride, 1-hydroxylbenzoltriazole, glycine-glycine-benzyl ester, dimethylformalmide, triethylamine, citric acid, NaOH, HCl, $CHCl_3$, CH_3OH, $CdCl_2 \cdot 2.5H_2O$ and Na_2S were purchased from Sigma-Aldrich and used without any further purification. All aqueous solutions were prepared with deionized H_2O (Milli-Q water, R>18.2MΩcm) and thoroughly bubbled by nitrogen to prevent oxidation.

2.2.2 Synthesis of Bionanotube Templates

Bionanotube templates in this report for the growth of CdS NWs were prepared from a glycine-based peptide monomer, bis(N-α-amidoglycylglycine)-1,7-heptane dicarboxylate. These peptide monomers (10 mM) were self-assembled into nanotubes in a pH 5.5 citric acid/NaOH solution after 1 week. These bionanotubes were grown in diameter of 100–400 nm, and the bionanotubes with an average diameter of 400 nm were separated with centrifugation and size separation columns. Details of the monomer synthesis, the self-assembly procedure, and the size separation are described in previous publications.[36, 42] After the bionanotubes were washed thoroughly with deionized water and followed by centrifugation for several times, these bionanotubes were redispersed in a phosphate buffer solution (pH=7.4) in a centrifuge tube. The resulting bionanotubes were used as templates for the immobilization of Cd^{2+} and the subsequent CdS nanocrystals growth.

2.2.3 Preparatoin of CdS nanowires

The assembly strategy of CdS nanocrystals (NCs) on the bionanotube is based on *in situ* two-step deposition procedure as illustrated in Scheme 1.Under nitrogen, 0.5mL cadmium chloride solution (7.0 mM) was added dropwise to 0.5mL bionanotube-containing solution to coordinate Cd^{2+} ions onto bionanotubes via electrostatic interaction. After stirred for 1 hour, the mixed solution was allowed sit for another 4 days in refrigerator at 4 ˚C. Then, the excess Cd^{2+} ions were removed by centrifugation (14,000 RPM 60minutes) and rinse by deionized water three times. In the second step, 0.5ml of freshly prepared oxygen-free Na_2S solution (2.0 mM) was added dropwise to this solution with vigorous stirring under N_2. The CdS NCs were formed on the bionanotube gradually during the following 48 hours incubation in refrigerator at 4˚C. Furthermore, these CdS NWs were ready for the optical and microscopic characterizations after purified by repeating centrifugation (14,000 RPM 60minutes) and rinse by de-ionized water three times for the removal of excess Cd^{2+} and S^{2-} ions since the residual ions could contaminate the coating. .

2.2.4 Instruments

Absorption spectra were recorded by a Cary 50 Probe UV-vis spectrophotometer in the wavelength range of 350-600 nm. The samples for PL characterization were prepared by transferring a 100 μL buffer solution containing CdS NWs onto a 10mm x 10mm Si(100) wafer, and then the sample was dried by spinning-coating. The steady-state photoluminescence (PL) emission spectra of these samples were recorded by a Jobin Yvon-Spex Fluorolog spectrophotometer equipped with a Xenon lamp as an excitation source at 367 nm. All measurements were performed at room temperature. Transmission Electron Microscopy (TEM) samples were prepared by dropping 10 μL of the sample solution on carbon-coated 300 mesh copper grids. Excess solutions were removed by filter papers. All TEM/HRTEM images and Selected Area Electron Diffraction (SAED) patterns were recorded with a JOEL JEM-2100 microscope operating at an acceleration voltage of 200 kV, equipped with a field emission gun. Energy-dispersive X-ray spectrometer (EDS) analysis was performed using a Thermo Noran EDX system attached to the JOEL JEM-2100 microscope.

2.3 Results and discussions

As illustrated in Scheme 2.1, the synthesis strategy consists of simple two steps. Pre-synthesized bionanotubes from self-assemblied peptide monomers, bis(N-α-amidoglycylglycine)-1,7-heptane dicarboxylate, was adjusted to pH 7.4 by phosphate buffer. Hence, -COOH groups from the bionanotubes are deprotonated at this pH and the resulting $-COO^-$ groups can coordinate with Cd^{2+} ions in the first step in Scheme 2.1. After the excess unbound Cd^{2+} ions were removed by centrifugation and rinsing procedures, S^{2-} ions were added from the precursor, Na_2S (2 mM), in the second step in Scheme 2.1 and the transparent solution containing Cd^{2+}-coordinating bionanotubes slowly turned the color of solution to light yellow. This color change suggests the formation of the CdS NWs in the solution.

Scheme 2.1 Scheme illustrated of *in situ* synthesis of CdS nanowires by using bionanotubes as templates.

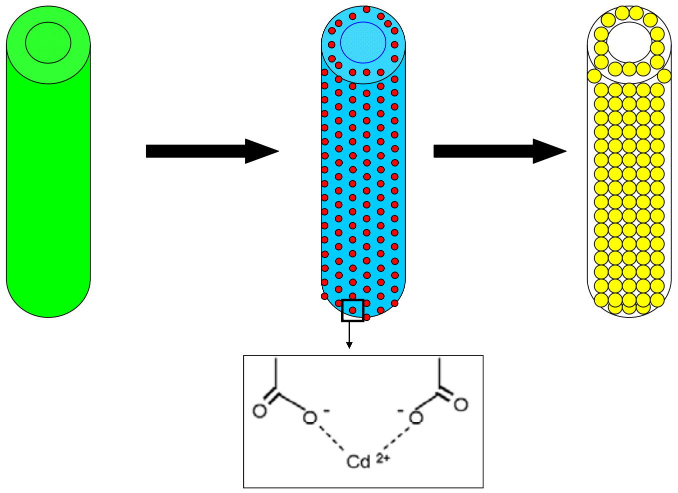

Fig. 2.1 (a) showed a typical TEM image of the resulting CdS NWs and an enlarged image of the selected area in Fig. 2.1 (b), respectively. These TEM images of CdS NWs clearly show uniform CdS NC coating on the surface of bionanotubes and the size of the CdS NCs on the bionanotubes are highly monodisperse. The CdS NCs have an average diameter of around 5.5 nm with a narrow size distribution on the basis of the TEM images. The average diameter of CdS NCs matches the distance between the two adjacent $-COO^-$ binding sites along the bionanotube axis, 6.4 nm, [36] which suggests that the $-COO^-$ groups may coordinate Cd^{2+} nucleation and the size of resulting CdS NCs is limited by this spacing. The CdS NCs on the bionanotube were further characterized by high-resolution TEM (HRTEM) (Fig. 2.1 (c)). The HRTEM image of CdS NCs shows a lattice fringe of d=0.332nm, corresponding to the (111) plane of CdS in the face-centered

cubic (fcc) structure.[30] In order to confirm the coating of CdS NCs on the surface of bionanotube, selected area electron diffraction (SAED) was conducted. In Fig. 2.1 (inset), SAED pattern of CdS NCs on the bionanotube shows crystalline faces of (111), (200), (220) and (311).[43] The elemental composition of the CdS NWs is further validated to contain C, O, P, S, Cu and Cd in the EDX spectrum of Fig. 2.2 The appearance of C and O element should be attributed to the bionanotube, whereas N could come from phosphate buffer and Cu is from the TEM grid.

The UV-vis spectroscopic measurement (Fig. 2.3) of CdS NWs shows an absorption peak at 438nm. This peak is blue-shifted about 77 nm from the absorption peak of bulk CdS crystals at 515nm. The absorption peak at 438 nm matches the peak of CdS NCs in a diameter of 5.3 nm. [34] The HRTEM image in Fig. 2.1 (b) also shows that the size of CdS NCs on the bionanotube is around 5.5 nm, and this agreement indicates that the absorption peak at 438 nm is from the independent CdS NCs and there is no electronic coupling between these NCs. The steady state photoluminescence spectrum reveals that the CdS NWs displayed its emission peak at 463 nm in Fig. 2.3. This peak also represents the intrinsic emission of the CdS NCs in a diameter of 5.5 nm coated on the surface of bionanotubes. A blue-shifted wavelegnth of 187 nm from bulk CdS crystals (Em.=~650nm) also provides concrete evidence that quantum-confinement of CdS NCs is in effect on the bionanotube templates. With the procedure in Scheme 2.1, CdS NCs were successfully produced on bionanotubes and the CdS NWs showed the characteristic photoluminescence of CdS NC domains. It is worth noting that 605 nm emission peak is absent in the CdS NW emission spectrum mostly originated from the transition of electrons between trapped surface states and the valence band of CdS. This transition is

Figure 2.1 (a) TEM image of a typical CdS NWs, scale bar: 1 μm. (b) enlarged image of selected area in (a), scale bar: 20 nm. (c) HRTEM image of selected area in (b), scale bar: 2 nm. (Inset) ED pattern of the nanowires.

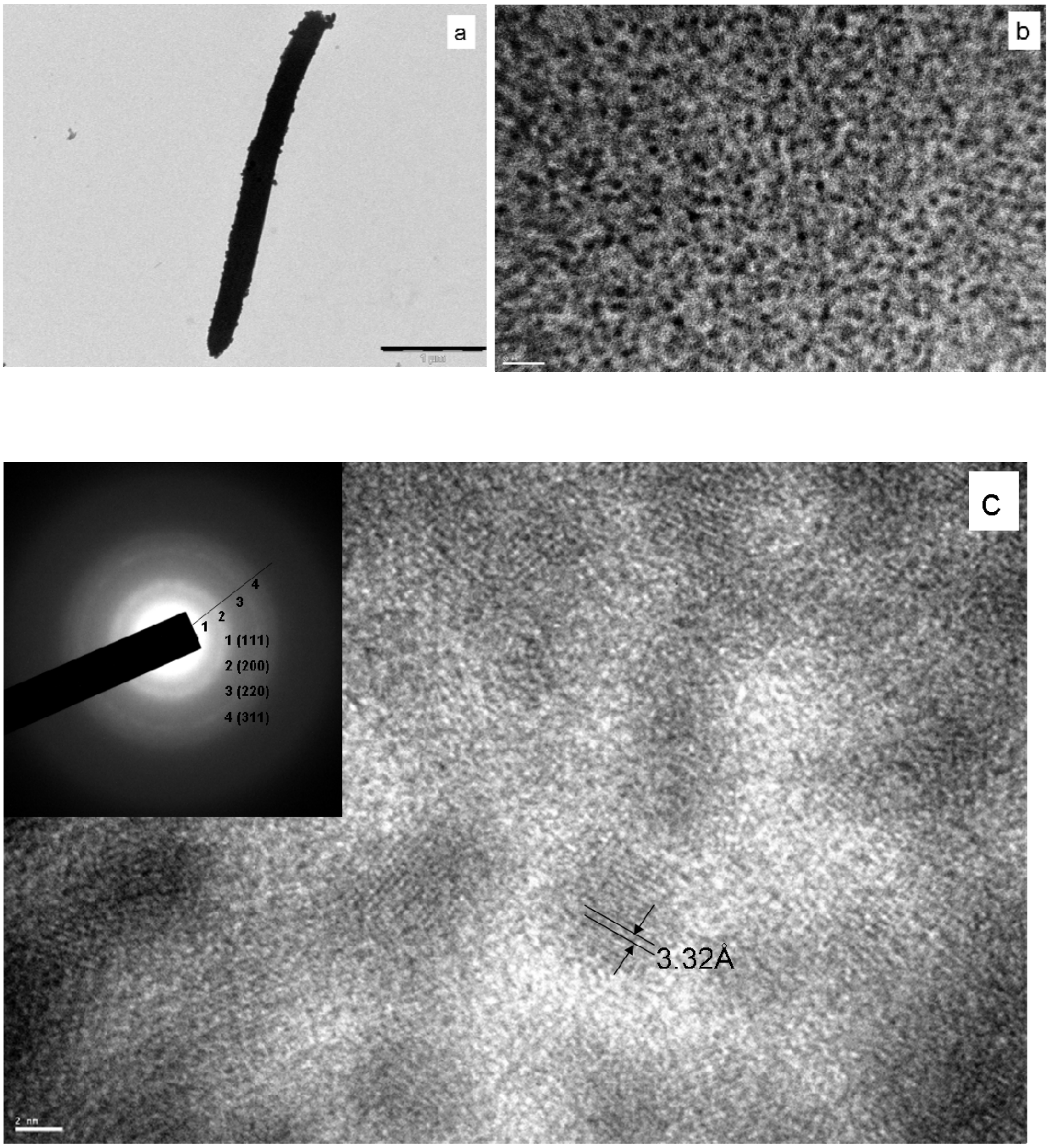

observed when the CdS contains to the large number of surface defects, [45] and the spectra in Fig. 2.3 shows that CdS NCs synthesized by this method have less defects due to the low growth speed in the second step in Scheme 2.1.

Figure 2.2 Energy-dispersive X-ray spectrometer spectrum of CdS nanowires

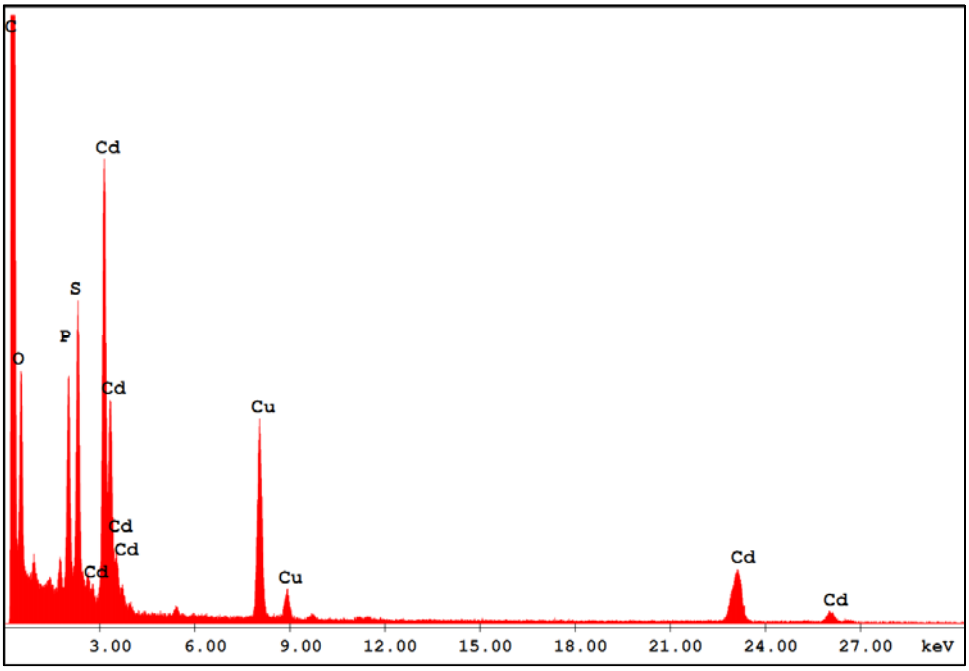

When three different concentrations of cadmium chloride precursor solution, 2 mM, 5mM and 10 mM, were used in the synthesis at the concentration of S^{2-} (2 mM) and incubation time of 6days (4 days for the first step and 2 days for the second step), only part of bionanotube surface was coated by CdS NCs at concentration of 2mM and 5mM (Fig. 2.4 (a), (b)) while at the high concentration of 10mM entire surface of the bionanotube is coated by CdS NCs (Fig. 2.4 (c)). This result suggests that few Cd^{2+} ions bind on the surface of bionanotube resulting less nucleation centers in the low concentration of Cd precusor. But when the concentration of Cd^{2+} was increased to 10 mM, the length of bionanotubes decreased dramatically from 4±0.6 µm (2mM, 5mM and 7mM) to 0.8±0.2 µm with high CdS nanocrystal coating on its surface (Fig. 2.4 b).

Figure 2.3 Room temperature UV-vis spectra of CdS nanowires (black curve) and PL spectra of CdS nanowires (red curve).

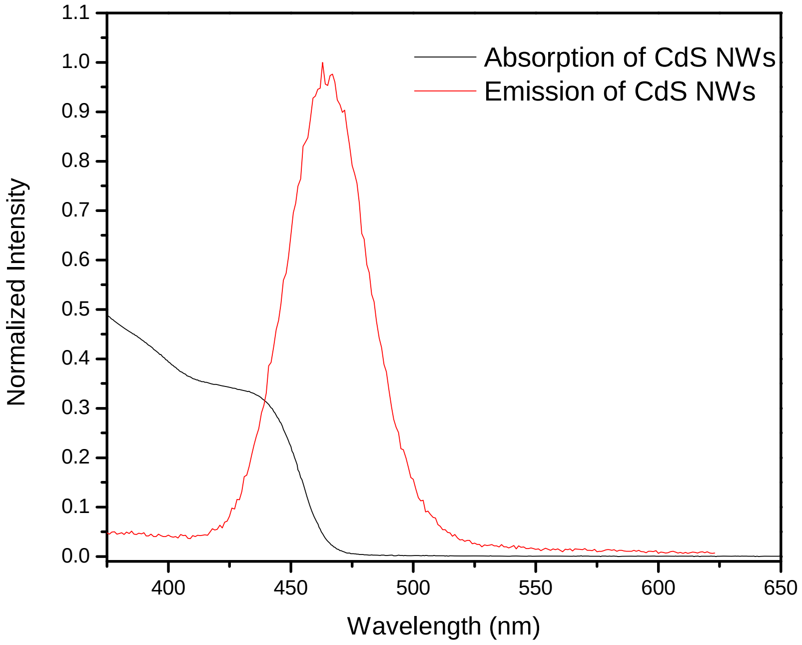

And the yield of final CdS NWs decreased almost 90% as compared with the yield of CdS NWs at the Cd^{2+} concentration of 10 mM. Obviously the CdS NWs prepared at the Cd^{2+} concentration of 7 mM showed the best morphology of resulting CdS NWs since the CdS NCs are packed in the compact arrangement on the whole surface of templating bionanotube.

Figure 2.4 (a) TEM image of CdS nanowires by using concentration $CdCl_2$ solution of 2 mM, scale bar: 2 μm. (b) TEM image of CdS nanowires by using concentration $CdCl_2$ solution of 5 mM, scale bar: 0.5 μm. (c) TEM image of CdS nanowires by using higher concentration $CdCl_2$ solution of 10 mM, scale bar: 1 μm.

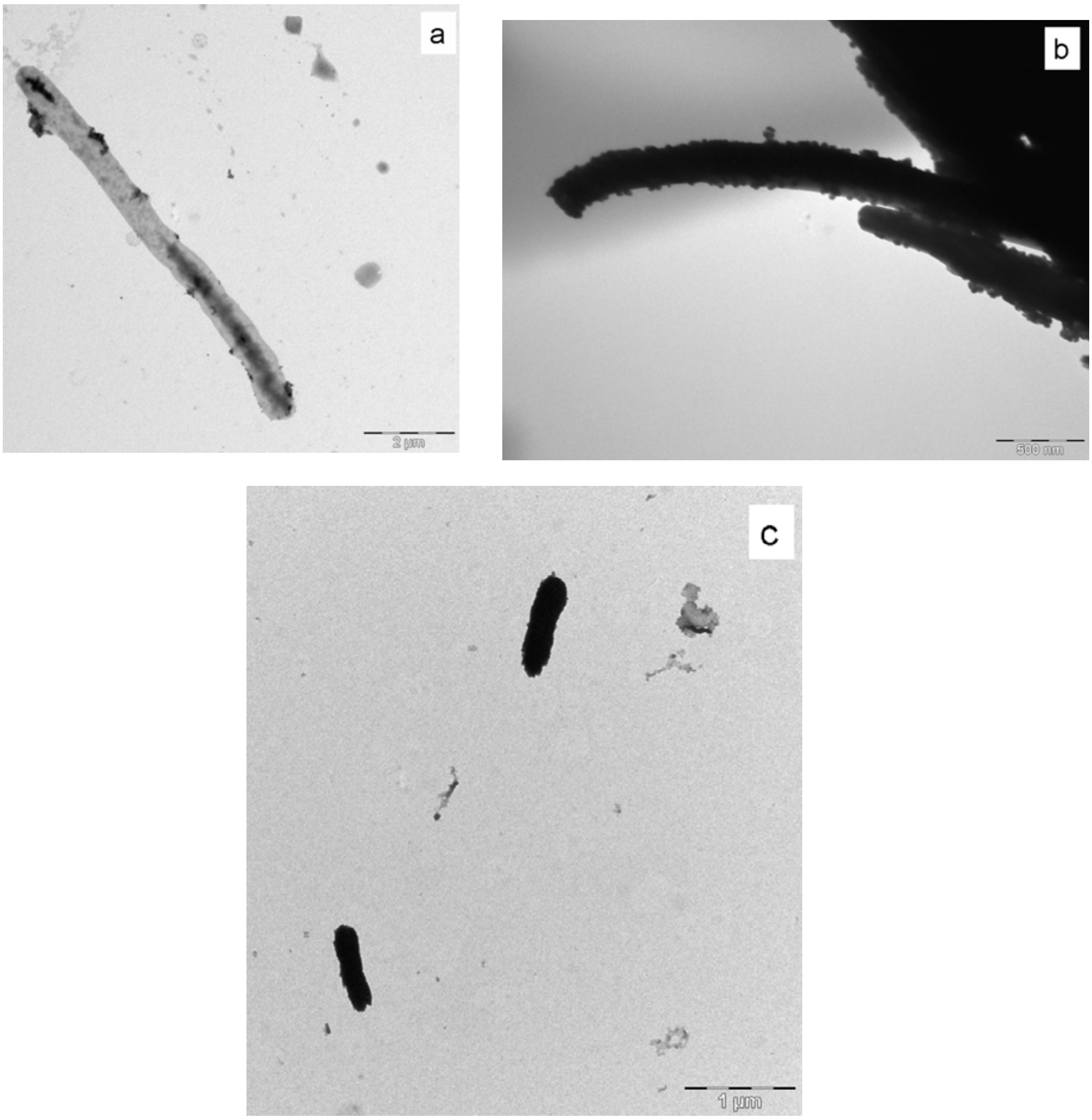

As a principal step in the whole synthesis procedures, it is worth mentioning that the optimal concentration of Cd^{2+} precursor is 7 mM. If the concentration of Cd^{2+} precursor was as low as 2 mM, not all -COO$^-$ groups from the bio-nanotube surface were able to coordinate with Cd^{2+} ions due to fewer amounts of Cd^{2+} ions in the mixture solution, which resulted in less growth centers on the bionanotube surface. Finally, only a small part of the bionanotubes surface was overcoated by formed CdS nanocrystals. On another hand, if high-concentrated Cd^{2+} precursor solution like 10 mM was used for incubation with bionanotubes, the bionanotube structures were decomposed by the high concentration Cd^{2+} in the mixture solution and truncated bionanotubes with much shorter length (less than 1 μm) were coated by CdS nanocrystals. The decomposition is because the high concentrated Cd^{2+} ions destroyed the hydrogen bonds network between bionanotube monomers. [30]

Figure 2.5 (a) TEM image of CdS nanowires by using 7mM $CdCl_2$ solution with incubation time of 1 day , scale bar: 1 μm. (b) TEM image of CdS nanowires by using 7mM $CdCl_2$ solution with incubation time of 2 day , scale bar: 1 μm.

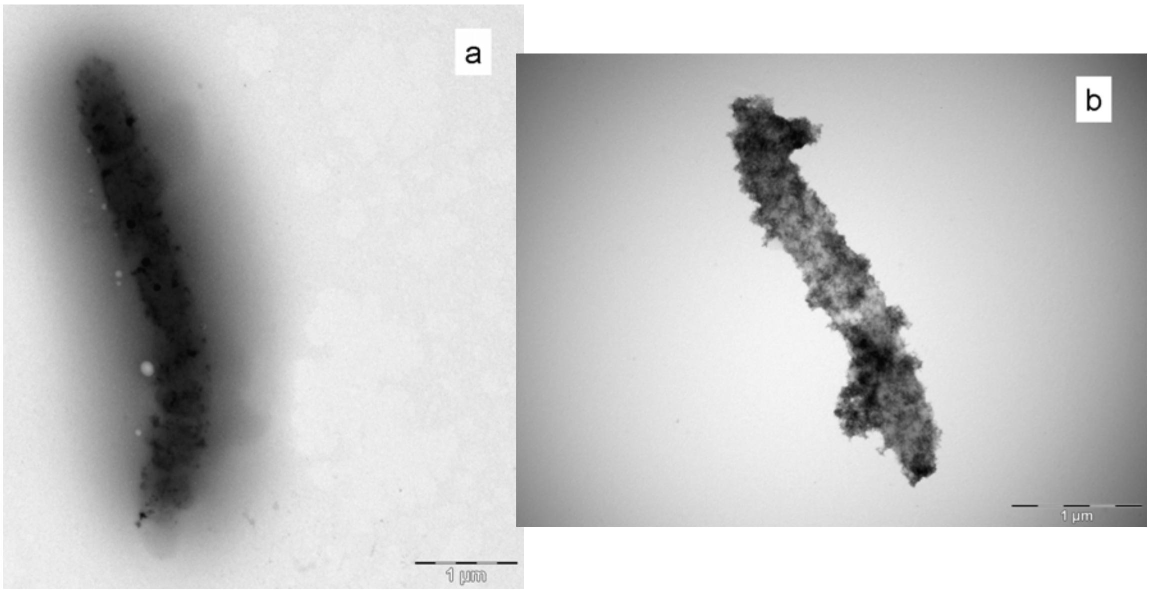

To further investigate the direct growth mechanism of CdS NCs on the surface of bionanotubes, we conducted another set of control experiments by varying the incubation time to 1 day and 2 days in the first step of reaction at the fixed Cd^{2+} precursor concentration of 7 mM. Figs. 2.5 (a) and (b) reveal the morphology difference of resulting CdS NWs which were characterized by TEM. Compared the 4 day-incubation as shown in Fig. 2.1 (a), these results suggested that the coating density of CdS NCs on the bionanotubes increases as the incubation time increases from 1day, 2days to 4days. Longer incubation time helps more Cd^{2+} ions anchored on the bionanotubes for the higher coating density of CdS NCs. Both control experiments with precursor concentration and incubation time changes indicate that the Cd^{2+} ion concentration is a key to control in the direct growth mechanism of CdS NCs on the bionanotubes. Another control experiment revealed that reaction between 7mM $CdCl_2$ and 2mM Na_2S without bionanotubes only produced aggregated CdS nanocrystals with diameter ~20nm which is shown in Fig. 2.6. This result indicates that the coordination between –COOH groups and Cd^{2+} ions play a critical role to decide the size of CdS nanocrystals in the whole synthesis procedure of CdS NWs.

It is worth noticing that this methodology has several advantages over conventional wet CdS NW synthesis methods such as a simple growth process and high crystallinity. The resulting CdS NCs on the bionanotube maintain discreet quantum confinement even when they are assembled in high density useful feature for future device applications.

Figure 2.6 TEM image of CdS nanocrystals from reaction between 7mM $CdCl_2$ solution and 2mM Na_2S solution without bionanotubes as templates, scale bar 100nm.

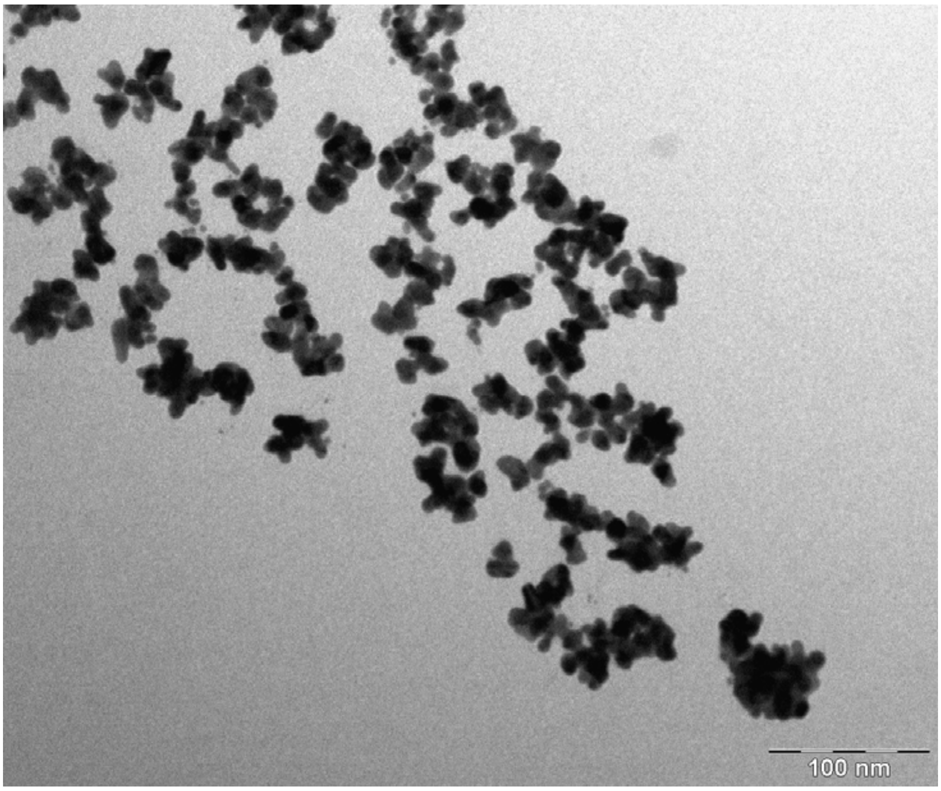

2.4 Conclusion

We have developed a novel bionanotube-templating CdS NW synthesis protocol at pH 7.4 and room temperature. The *in situ* growth mechanism is in two steps: first Cd^{2+} ions from $CdCl_2$ precursor solution are anchored on bionantubes at $–COO^-$ groups via electrostatic interactions. Then, CdS NCs are grown upon the addition of Na_2S solution. Both Cd^{2+} concentration and incubation time are important to control the morphology of resulting CdS NWs. This outcome may lead the potential applications of bionanotubes to serve as the templates for the growths of various metal/semiconductor NWs whose electronic properties depend on the size of NCs on the NWs.

Chapter 3. Optical Microcavity Building Based on Type I-II QD Assembly

3.1 Introduction

Scientists have paid much effort on building optical resonators which are a major component of lasers after the report of the first laser in 1960.[46] Diverse applications of optical resonator have been realized from both fundamental and industrial studies and keep growing continuously. The development of such photonic devices followed the trend towards miniaturization and already reached a level of dealing with single colloidal nanocrystal. Microcavities are very powerful micro-structures to control the optical properties of nanosized emitters at the quantum scale by assembling them into macro-sized cavities. [47, 48, 49, 50] It is well known that there are three basic designs of microcavities: 1, classical configurations using distributed Bragg reflectors (DBR). [51] It is a structure formed from multiple layers of alternating materials with varying refractive index and each layer boundary causes a partial reflection of an optical wave. 2, metallic mirrors via microtoroids which usually is an array of small ring-shaped structures on the surface of a semiconductor substrate. [52] 3, photonic crystal-based cavities. [53] In particular, the first photonic resonator devices already optimized by changing the material composition and modifying the thickness of DBR layer offered excellent performance.

Quantum dots (QDs) are highly fluorescent colloidal semiconductor nanoparticles which are typically less than 10nm in diameter. [54] Their unique optical properties such as broad absorption region, tunable size-dependant photoluminescence (PL), high quantum yield (QY) and narrow emission peaks [55, 56] compared with other fluorophores render them promising materials for photonics applications such as organic–inorganic hybrid solar cells, [57] white-light lasers and energy converters. [58, 59, 60, 61] Embedding QDs into these microcavities allows to take advantage of the sharp emission bands as well as the large oscillator strengths and to provide an efficient guide for this luminescence through the confined electromagnetic modes of the cavity.

Several attempts have been reported to incorporate QDs in photonic structures with various approaches, including QDs embedded in polymethylmethacrylate spheres, [62] polystyrene micro-spheres, [63] one-dimensional microcavities, [64, 65] and opal photonic crystals.[66, 67, 68] An enhancement of the spontaneous emission rate [69, 70] and strong coupling between the QD-exciton and the photon cavity mode are desirable to accomplish, [71] however the enhancement of the spontaneous emission has not yet been demonstrated, mainly because of the larger size of the QD-organic hybrid structures as compared to the visible emission wavelength of the QDs.

Here, we examined the study to build a novel microcavity by embedding two types of QDs, type I CdSe-ZnS (QD491) and type II CdS-ZnSe (QD560), between two DBRs (formed by alternating SiO_2 and Si_3N_4 layers). The spontaneous emission of QDs embedded inside a quasi one-dimensional microcavity should be further enhanced by fluorescence resonant energy transfer (FRET) from the donor of QD491 to the acceptor of QD560 (The FRET between QD491-QD560 in solid state phase was studied and reported in Chapter 1).

3.2 Experiments and instruments

The type I CdSe-ZnS (QD491) and type II CdS-ZnSe (QD560) QDs in this report were prepared by using a stepwise procedure composing of core nano-crystals growth (CdSe, CdS respectively), shell over-coating (ZnS, ZnSe respectively), TOP/TOPO-capping, size selection precipitation and final purification. [72, 73, 74, 75]

3.2.1 Synthesis of CdSe-ZnS type I QD (QD491)

3.2.1.1 Synthesis of CdSe cores

First, 51.4 mg (0.4 mmol) of CdO (Aldrich) was placed into a flask containing 1.15 mL (1.045g) of Trioctylphosphane oxide (TOPO, 99%; Aldrich) and then it was mixed with 2.85 mL (2.375g) of hexadecylamine (HDA, 98%; Aldrich) at 270 °C under nitrogen flow. After 230 µL (0.8 mmol) of dodecylphosphonic acid was added, and the temperature of the resulting colorless solution was raised to 250 °C, 3.5 mL of a 0.2 M solution of Se (Aldrich) powder in trioctylphosphane (TOP) (97%; Aldrich) was quickly injected. The reaction was stopped after 45 seconds by pouring the mixture into 30mL methanol (Aldrich) at room temperature. The CdSe cores were purified by methanol rinsing and centrifugation (14,000 RPM, 15 minutes) and finally re-dispersed into hexane (Aldrich).

3.2.1.2 Coating ZnS shell onto CdSe cores

First, 14 g Trioctylphosphane oxide (TOPO) (99%; Aldrich), 3 mL oleylamine (99%;

Aldrich), 2 mL HDA (98%; Aldrich), and 2.0 mmol bis(2,4,4-trimethylpentyl)phosphinic acid (BTMPPA, 99%; Aldrich) were degassed under vacuum for 2 hrs in a three-necked flask at 100°C. The CdSe cores dispersed in hexane from previous synthesis were added to the degassed solution and the hexane was removed at 80°C under vacuum. Under a flow of argon, the mixed solution was heated at 180°C and the ZnS shell precursor solution (0.1mmol diethylzinc (95%; Aldrich) and 0.1mmol hexamethyldisilthiane (>97%; Fluka) dissolved in 7 mL TOP) was added dropwise. After the addition was complete, the solution was kept at 180°C for 5 min and then left stirring overnight at 75°C to anneal the ZnS shell. The resulting CdSe-ZnS core-shell QDs were purified by precipitation in methanol, same as the core-purification procedure. The final QDs were re-dispersed into hexane.

3.2.2 Synthesis of CdS/ZnSe type II QDs (QD560)

3.2.2.1 Synthesis of CdS cores

The Cd precursor solution was prepared by mixing a degassed (under vacuum at 100°C for 1 h) solution of cadmium acetate hydrate (1 mmol), trioctylphosphane (TOP) (6 mL), and bis(2,4,4-trimethylpentyl)phosphinic acid (BTMPPA) (1 mmol) with a degassed (under vacuum at room temperature for 1 h) solution of elemental sulfur (1 mmol, Aldrich) in oleylamine (3 mL, Aldrich). The resulting solution was rapidly injected into a round-bottomed flask containing degassed (under vacuum at 100°C for 1 h) oleylamine (7 mL, 98%) and trioctylphosphane (TOP) (8 mL) stirring rapidly at 250–280°C. After QDs were grown at 250°C for 15 to 30 min, the heating was stopped and cooled down by removing the heating source. Before coating the ZnS shell, the CdS cores were precipitated out of the growth solution and then separated from hexane solution one more time to remove unreacted precursors and excess capping ligands. The particles were flocculated from the growth solution by adding 0.4 equiv of hexane, 0.8 equiv of butanol, and 3 equiv of methanol (total 100mL) to 1 equiv of growth solution (24mL) and centrifuged for 15 min at 14,000 RPM. The particles were then dispersed in hexane and flocculated by adding one drop of butanol per equivalent of original growth solution and 0.5 equiv of methanol, and then centrifuged for 15 min. The CdS core nanoparticles were finally re-dispersed in pure hexane.

3.2.2.2 Coating of ZnSe shell onto CdS cores

A colloidal solution of ca. 20 mg of CdS cores was placed in a three-neck flask under purified argon flow. After adding 2.5 mL of TOPO with 1.5 mL of HDA, the mixture is heated at 190 °C and then kept at this temperature evaporate hexane completely. Zinc stearate (316 mg, 98%; Aldrich) was dissolved in 2.5 mL of toluene upon gentle heating (ca. 60 °C). After cooling to room temperature, the resulting 0.2 M solution is mixed with 2.5 mL of a 0.2 M solution of Se in TOP. This mixture was injected with a syringe pump within 1 hr into the reaction flask containing the CdS core nanocrystals at 190 °C. Periodically small aliquots were removed in order to monitor the shell growth by TEM. After the addition was completed, the resulting crystals were annealed at 190 °C for an additional 1-1.5 hrs. The core-shell QDs were purified by the precipitation method same as the core-processing procedure. The final CdS-ZnSe type II QDs were re-dispersed into hexane.

The CdSe core of CdSe-ZnS type I QDs (QD491) has diameters of 3.9±0.1 nm determined by transmission electron microscopy (TEM). The thickness of ZnS shell on the CdSe core is around 1 nm. The diameter of CdS core in the CdS-ZnSe (QD560) type II QDs is 4.0±0.3 nm and the thickness of ZnSe shell is around 1 nm.

3.2.3 Instruments

The steady-state fluorescence spectra were acquired by a Jobin Yvon-Spex Fluorolog spectrometer with a Xenon lamp as an excitation source at 367 nm. Absorption spectra were recorded by a Cary 50 Probe UV-vis spectrophotometer in the wavelength range of 400-700 nm. The micro-cavity structures were grown by Plasma-enhanced chemical vapor deposition (PECVD) with NH_3, N_2O and SiH_4 as precursor vapors. All TEM samples were studied by Zeiss EM 920 Transmission Electron Microscope at an acceleration voltage of 80 kV.

3.3 Discussions

The cavity is composed of SiO_2 layer with a thickness of a half-wavelength of emission light (560nm) sandwiched between two identical top and bottom DBRs. Each DBR consists of six periods (12 layers) of alternating SiO_2/Si_3N_4 layer (96.6nm for SiO_2 layer and 79.1nm for Si_3N_4 layer, respectively) as illustrated in Scheme 3.1.

Scheme 3.1 Scheme of optical microcavity design.

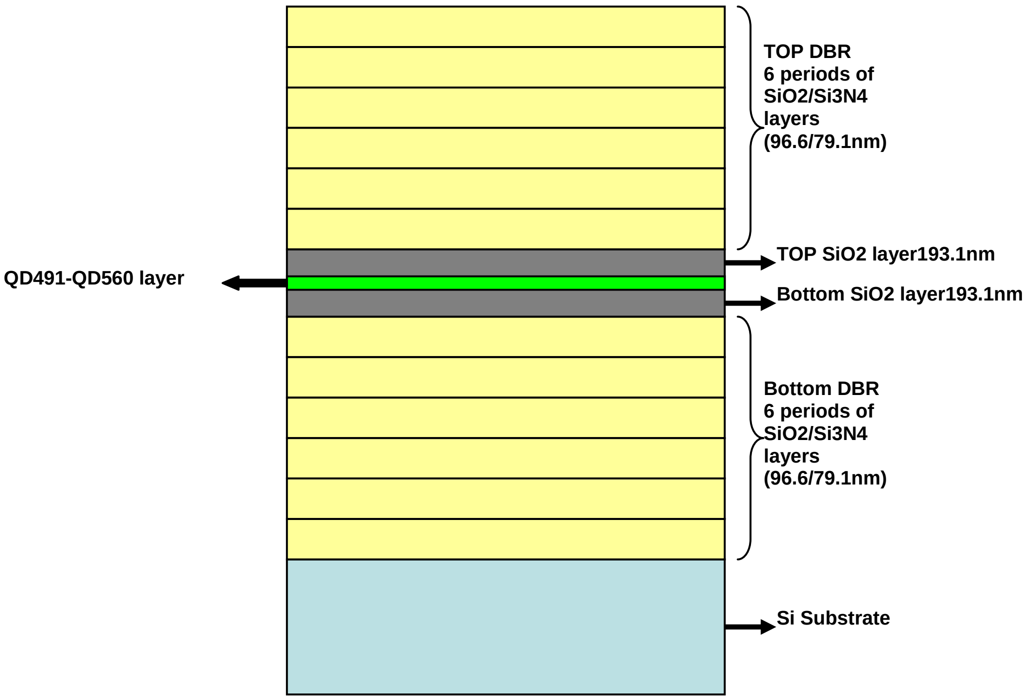

The bottom SiO_2 layer deposited on the top of bottom DBR established the first half of the cavity. Then, the QD491-QD560 FRET assembly layer was spin coated by 100 µL of QD491-QD560 mixed QD solution (QD491 concentration: $6.0x10^{-7}$ M, QD560 concentration: $1.2x10^{-7}$ M. QD491-QD560 molar ratio: 5:1) onto the first half of the cavity at 100RPM for 360 seconds. The resulting solid samples were placed in a 40 ˚C oven for 1 hr to remove the trace amount of organic solvent. The photoemission was measured in order to check the coating quality of QD layer before and after depositing the top half of the SiO2 layer onto the QD layer. The top DBR is deposited if the intensity of both PL spectra is consistent.

Figure 3.1 (a) Photoluminescence band of QD491-QD560 QD layer spun coat on the bottom half of microcavity. (b) Optical property of QD491-QD560 QD as synthesized.

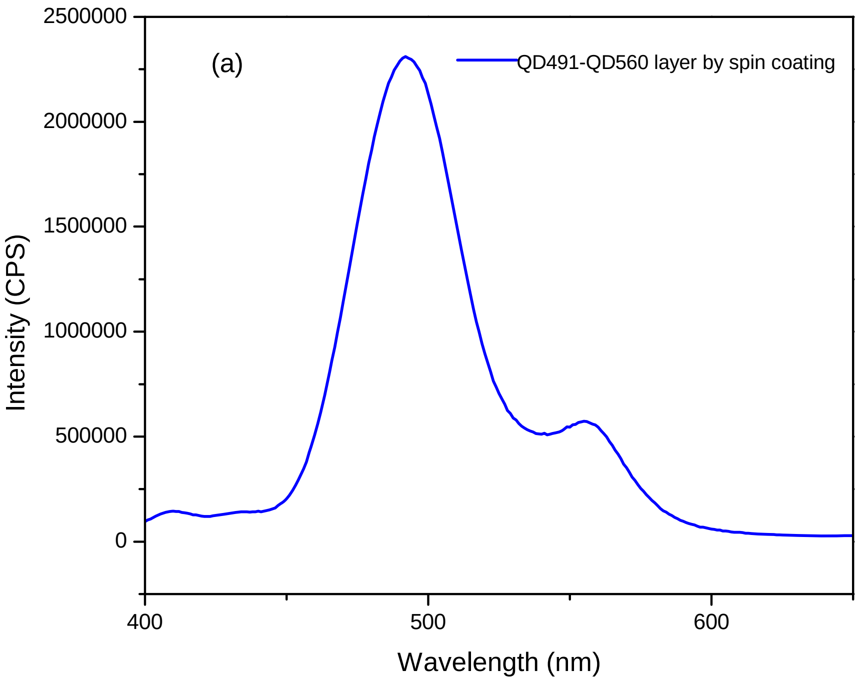

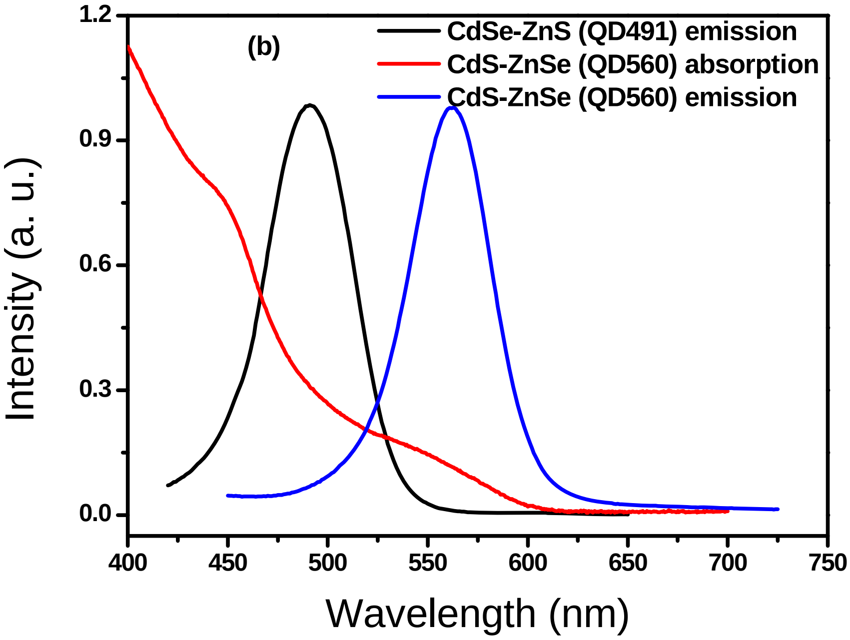

A piece of 10mm x 10mm silicon substrate for the cavity was rinsed by acetone under ambient atmosphere and dried by pure nitrogen gas. After successful spin-coating of the QDs layer onto the bottom half of the cavity, the PL measurement of the QD layer as shown in Fig. 3.1-a. The optical properties of synthesized QD491 and QD560 are shown in Fig. 3.1-b. The spin coating of mixed QDs onto silicon substrate is successful which is verified directly by comparing PL spectrum of free QD sample (shown in Fig. 3.1-b) with that of the mixed QD sample after coating (shown in Fig. 3.1-a). The PL spectrum of mixed QD sample after coating shows two peaks of 491nm and 560nm which are corresponding to the emission peaks of free QD491 and QD560 QDs. After this verification step, the top SiO_2 layer was coated on the QD layer at 250 °C by PECVD. The emission spectrum of the resulting cavity in Fig. 3.2 shows that intensity from type I QD is decreased almost 100 fold and the peak from type II QD totally disappears from the spectrum. The tremendous quenching of the photoluminescence indicates that the QD structures were damaged during the depositing of a top half SiO_2 layer. We hypothesize two possible reasons for this change: 1. high temperature (250 °C) from the SiO_2 coating reaction in the PECVD chamber; 2. high energy plasma atmosphere in the PECVD chamber.

Because the CVD chamber temperature (250 °C) is much higher than the temperature to grow coating of ZnS on CdSe cores (180 °C) or coating of ZnSe on CdS cores (190 °C), the high temperature inside the chamber could melt down the shell materials of both QD491 and QD560 and play a factor to damage the QD structure.

Figure 3.2 Photoluminescence of QDs after depositing of top SiO_2 layer by PECVD at 250°C.

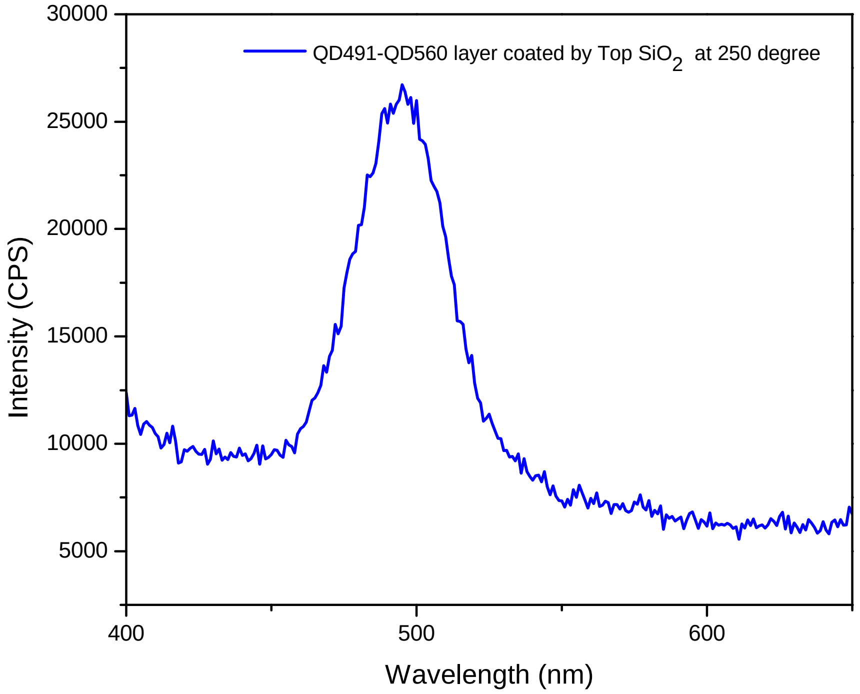

In order to examine this hypothesis, we did a control experiment by heating the mixed QDs spin-coated on Si substrate at 150°C on a hot plate for 360 seconds and then check its PL spectrum. Since the intensity of QDs photoluminescence in Fig. 3.3 is not quenched as much as the intensity measured in the previous sample treated with PECVD, it is concluded that these QDs are stable at 150°C. So, the high temperature is not the major factor to damage the QD structures as far as the chamber temperature is not higher than 150°C.

Figure 3.3 Photoluminescence of QDs after heated for 360 seconds on a 150°C hot plate.

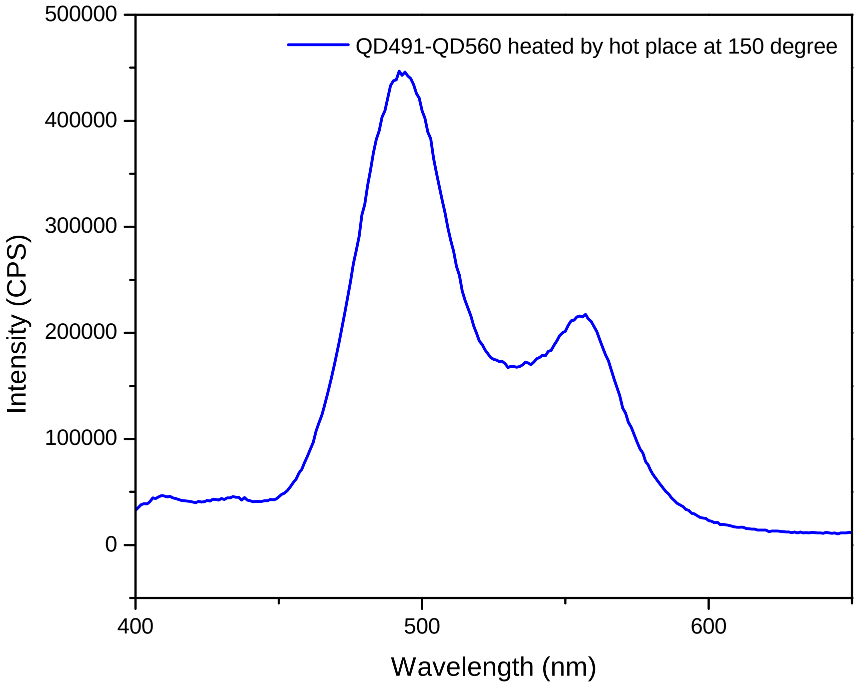

On the basis of above result, the major reason of photoluminescence quenching is the high energy plasma in the PECVD chamber. In order to examine whether the high energy plasma atmosphere in the CVD chamber is the reason to damage the core-shell structure of QDs, the top SiO_2 layer was deposited at the reaction temperature of 150 °C in the PECVD. The PL spectrum of QDs in this sample (Fig. 3.4) shows that the intensity of photoluminescence is quenched in the same magnitude as shown in Fig. 3.2. Because this reaction temperature is lower than the one in Fig. 3.2 but equivalent with the one in Fig. 3.3, the major reason of the photoluminescence quenching in the QD cavity is due to the high energy plasma in the PECVD chamber.

Figure 3.4 Photoluminescence of QDs after depositing of top SiO_2 layer by PECVD at 150°C.

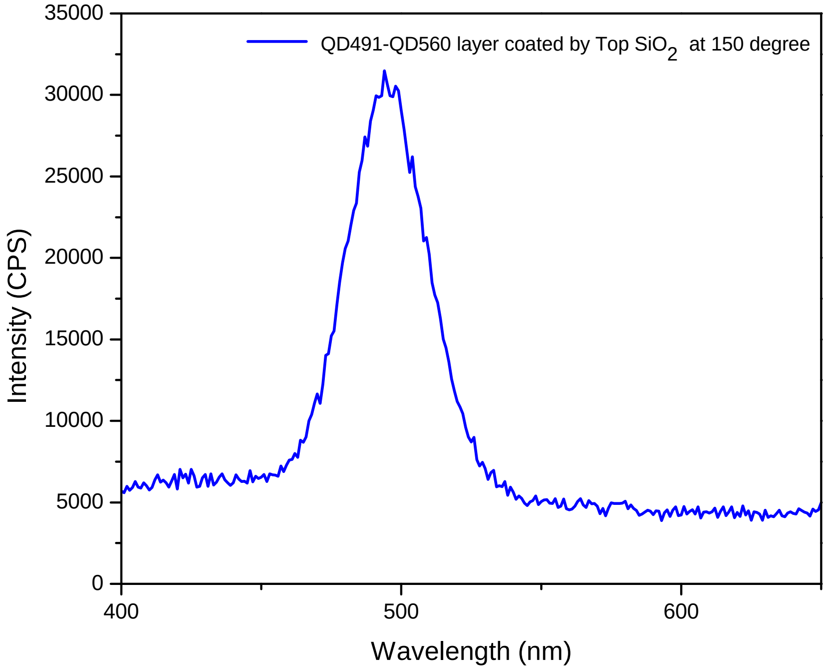

It has been reported that the electron energy distribution for this type of RF glow discharge is described by a Maxwellian distribution over the energy range 0.1-15 eV [76] and even a typical average value of electron energy is in the range of 2-4 eV, in some cases as high as 30 eV. [77] Collisions of these high-energy electrons with molecules of gas precursors (N_2O and SiH_4) will produce reacting species such as radicals (SiH_3, SiH_2, SiH, etc) and atoms (Si, H) from the dissociation of precursor molecules.

During the SiO_2 depositing process, reactive species generated by the plasma may etch the shell materials (ZnS and ZnSe) of the QDs and eventually the structure of QDs could be damaged and the PL intensity is quenched dramatically. Another hypothesis is that the PL property of QDs could be damaged by "photo-bleach mechanism". [78] The species generated by the plasma with energy higher than 3eV could excite the both QD491 and QD560 intensively and continuously, which results in expiration of QD emissions in a few minutes.

It is clear that in order for the prevention of damaging QDs structures, following two critical requirements should be met in future experiments: 1. the reaction temperature should not be raised higher than 150°C in the PECVD chamber to avoid melting down the shell materials of QDs; 2. the mixed QDs need to be prepared by re-dispersing QDs into different solvents like poly(methyl methacrylate) (PMMA) instead of hexane. QDs stabilized with TOPO are soluble in methyl methacrylate (MMA), which is widely used for the synthesis of PMMA, a solid organic glass. [79] We select this polymer as the material for photonic dot preparation because of its low photoluminescence background and high transparency in the ultraviolet wavelength, which allows the excitation of embedded QDs in their characterization. PMMA will serve as a protective matrix layer for the QDs from contacting the plasma species to minimize both “plasma etching” and “photo bleach” damaging to the QD structure.

Chapter 4. Interfacial Templating of Inorganic Nanostructures Using a Growth Directing and Reducing Peptide

4.1 Introduction

Biological organisms synthesize organic-inorganic hybrid materials into complex nanostructures by coupling self-assembly of the organic phase with the ability to direct growth of the inorganic phase[80, 81, 82, 83]. This mechanism has inspired engineers to develop hybrid materials at the nanometre scale, where the properties of metals and semiconductors show unique electronic, optic, and catalytic properties[84, 85]. Several methodologies have been developed to engineer functional nanoscale materials. Although, in order to precisely engineer materials with hierarchical length scales, top-down approaches are typically applied, which are limited by cost or availability of short wavelength lasers. An alternative is using bottom-up techniques to arrange atoms into nanostructures, which is limited by the complexity of structures accessible. Our work is inspired by biological composite materials where both nanoscale features and complexity are realized through non-equilibrium assembly processes[86].

One well-established bottom-up methodology applied citrate reductants to form simple spherical gold nanoparticles[87], but anisotropic nanoparticles such as nanorods[88, 89], nanocubes[90], triangular platelets[91], and nanostars[92] have also been observed using seed mediated approaches that use strong reductants to produce the initial seed, increasing issues with toxicity and expense, therefore the use of biomimetic systems circumventing these issues may be an efficient pathway[93, 94]. In contrast, biomimetic templating agents have guided the assembly of particles into more complex structures such as nanochains[95] and double helices[96].

There are several peptide-based approaches to facilitate synthesis of inorganic materials by templates[97, 98, 99, 100]. In the case of gold, histidine-rich peptides have been applied to decorate the shell of nanotubes[101], templating a shell of isotropic gold nanoparticles along the perimeter. Also, reports exist of -sheet forming peptides that self-assemble into fibres producing laterally spaced linear nanoparticle arrays based on the location of charged residues within the fibril[102, 103]. However, in most cases, the inorganic nanoparticles are formed by using reducing agents prior to exposure to the organic template. Recently, tryptophan has been used as a non-toxic method to synthesize spherical nanoparticles at room temperatures and anisotropic particles at higher temperatures[104]. Also, Slocik *et. al.* report a one pot synthesis of spherical particles using a peptide with biomolecular recognition properties[105]. Similarly, gold nanoparticles of multiple sizes and shapes have been synthesized *in situ* using peptide amphiphile hydrogels[106] and lemongrass extract has been used to generate triangular platelets[107].

We show that we are able to control both morphology and crystallinity as a function of surface pressure by using a peptide molecule that self-assembles at the air-water interface and is capable of reducing gold ions and coordinating them to form triangular nanoplatelets and related structures. Other two-dimensional techniques that template gold at different surface pressures involve polymers[108], lipids[109], and diacetylene[110] molecules, each requiring the formation of the nanoparticles prior to the self-assembly of the respective molecules. Therefore, our system explores a template that is capable of reducing and coordinating gold-ions from the subphase to explore the template

Figure 4.1 The peptide molecules Beta 9H and Beta 3 using van der Waals representation. (by Lorraine Leon)

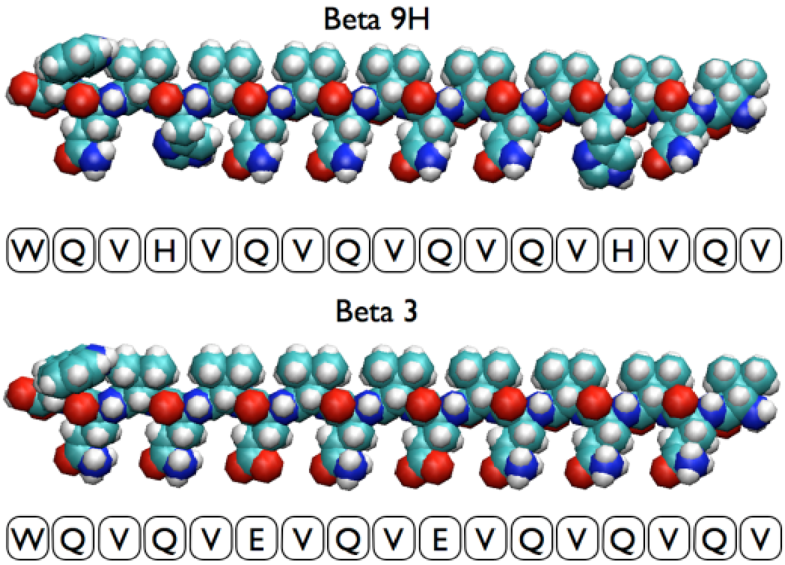

behaviour out of equilibrium, yielding varying shapes and crystallinity by simply controlling surface pressure without using high temperatures, reducing agents, or previously formed templates.

4.2 Experimental

Peptide molecules are synthesized by AnaSpec (San Jose, CA) with a purity of >80%. The peptides are stored at -20°C. Trifluoroacetic Acid, Chloroform, hexadecane, and carbon tetrachloride are obtained from Fisher Scientific (Pittsburgh, PA) and water is purified using a Millipore apparatus (Billerica, MA). Monolayers of the peptides are prepared by spreading a fresh solution of the peptide in trifluoroacetic acid/chloroform (1:9 v/v) at a concentration of 1mg/mL on a subphase of deionized water. Hydrogen tetrachloroaurate(III) is obtained from Sigma-Aldrich (Saint Louis, MO) Stock solution of hydrogen tetrachloroaurate(III) is freshly prepared at a concentration of 0.04 M and stored covered in foil at 4°C. Octadecyltrichlorosilane is obtained from Acros Organics (Thermo Fisher Scientific, Waltham, MA). Surface pressure-area isotherms are obtained using a KSV minimicro trough (KSV instruments, Helsinki, Finland). The peptides are deposited on a subphase of deionized water and are all compressed at the same speed of 5mm/min. Brewster angle microscopy images are obtained simultaneously with the surface pressure-area isotherms using an I-Elli 2000 ellipsometer/Brewster angle microscope (Nanofilm, Halcyonics, Gottingen, Germany). The resolution of the I-Elli 2000 is 1 μm in all images shown. Images are obtained before and after crystallization experiments.

Transmission Electron Microscopy (TEM) samples are prepared by taking from the air-water interface using a Langmuir-Schaefer technique onto carbon-coated copper grids. Excess solutions are removed by filter papers. These samples are then studied by TEM and electron diffraction (JOEL JEM-2100 Transmission Electron Microscope) at an acceleration voltage of 200 kV. Samples for the atomic force microscope (AFM) are obtained by transferring the peptide/gold monolayer using a Langmuir-Schaefer deposition technique using a silicon substrate that was previously coated with octadecyltrichlorosilane. The hydrophobic modification of the silicon substrate is achieved by using a procedure outlined previously by Kumar et al[124]. The presence of a hydrophobic layer is confirmed by measuring the contact angle, which is greater than 90°. Atomic force microscopy images are obtained using a Nanscope III instrument (Digital Instruments, Santa Barbara, CA) in tapping mode using Nanoprobe SPM (Santa

Barbara, CA) tips with a resonance frequency range of 307-374 kHz and a length of 125 μm.

Monolayers of the peptide molecules are compressed to a given surface pressure and then 80 μL of the 0.04 M hydrogen tetrachloroaurate(III) stock solution is added to the 50mL deionized water subphase using the injection port below the air/water interface. The ions are allowed to incubate for 10 hours before samples are taken using a Langmuir-Schaefer deposition technique using carbon coated 200 mesh copper grids from Electron Microscopy Sciences (Hatfield, PA).

Figure 4.2 The surface pressure/ area isotherm and Brewster angle microscopy images (width = 220 μm) obtained for Beta 9H at a temperature of 25°C on a deionized water subphase (pH~5.5). (by Lorraine Leon)

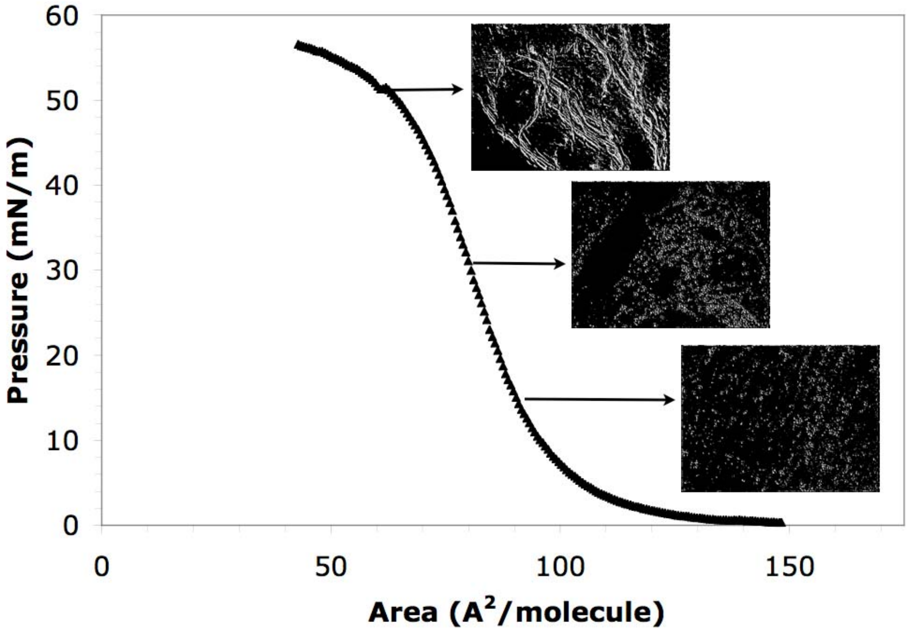

4.3 Results and Discussion

Langmuir Blodgett techniques are used to accurately characterize the self-assembly of the peptide, Beta 9H, at the air-water interface. The peptide molecule, shown in figure 4.1, is rationally designed to form a -sheet at the air-water interface. This design is accomplished by choosing amino acids with a high propensity to form a β-sheet[111] configuration, and the periodic sequence also defines an amphiphilic architecture, allowing us to confine the peptides to the air-water interface[112]. In addition to using an alternating hydrophobic and hydrophilic sequence of amino acids to achieve the periodicity associated with a β-sheet secondary structure, two other amino acids tryptophan and histidine are incorporated in this sequence. Tryptophan is included to reduce gold ions through the transfer of electrons from the amine group of Trp to the Au^{3+} ion[104]. Histidine is included in the sequence because of its ability to form complexes with metal ions using the imidazole and amine group of sequenced peptides[101, 113, 114]. To verify the role that histidine plays in the process of forming gold nanoparticles, we also use a peptide called Beta 3 that does not contain histidine, but still contains the tryptophan residue. The sequence and structure of the Beta 3 molecule is also shown in figure 4.1. The self-assembly of both these molecules under two dimensional confinement has been described previously using thermodynamic models for the surface pressure-area isotherms and phase behaviour[115]. In that paper, we describe how both Beta 9H and Beta 3 are surface active and form circular domains at low surface pressures and fibrous domains at high surface pressures. The isotherms and Brewster angle microscopy images of the phase behaviour of Beta 9H are shown in figure 4.2.

Figure 4.3 Brewster angle microscopy images taken at a surface pressure of 30mN/m (a) before incubation with Au^{3+} ions (b) after incubation with Au^{3+} ions. The width of the images is 220 µm. (by Lorraine Leon)

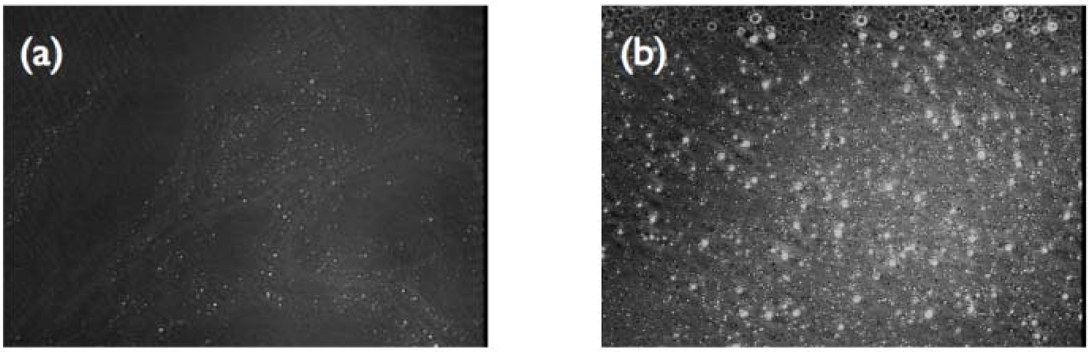

In order to investigate the ability of Beta 9H to form gold nanoparticles, the peptide is deposited on the air-water interface and compressed to different surface pressures after which solutions of $HAuCl_4$ are injected into the subphase using an injection port below the interface. During the experiment, the interface is visualized using a Brewster angle microscope. The Au^{3+} ions are left to incubate in the Langmuir trough for a period of 10 hours. Brewster Angle microscopy images of the interface with the peptide at a surface pressure of 30mN/m before and after the 10-hour incubation period are shown in figure 4.3. The images show that the Beta 9H peptide forms discrete domains before the addition of gold and that the interface considerably brightens as interfacial gold structures form during the 10-hour incubation period.

Brewster angle microscopy is a measure of changes of indices of refraction at the air-water interface, and the increased brightness indicates that a material of higher refractive index has formed on the interface [116]. In order to probe the nature of these structures found on the interface after the incubation period, samples are taken from the air-water interface using a Langmuir-Schaefer technique onto carbon-coated copper Transmission Electron Microscopy (TEM) grids. The TEM images obtained are shown in figure 4.4

with their corresponding electron diffraction patterns.

The images and diffraction patterns in figure 4.4 show samples collected at 30mN/m, 40mN/m, and 50mN/m. The image collected at 30mN/m shows an equilateral triangle with sides of approximately 800 nm. The corresponding electron diffraction pattern indicates that the triangle is a single crystal of hexagonal symmetry and can be indexed using the fcc structure of gold. The hexagonal pattern arising in the diffraction indicates that {111} facets bound the crystal[117, 118]. The strongest peaks obtained are for the peaks pertaining to the {220} reflections as seen in figure 4.4a.

At 40mN/m, figure 4.4 indicates that the triangular crystal formed is rougher and smaller with sides of approximately 510 nm. The diffraction pattern still has hexagonal symmetry similar to that of the triangle formed at 30mN/m. However, the electron diffraction pattern has small differences to that shown for 30mN/m. There are often coupled diffraction peaks in the place of a single diffraction spot, suggesting that the rougher triangle is made up of multiple single crystals that are formed out of phase.

Figure 4.4 The TEM images and corresponding electron diffraction patterns at varying surface pressures: (a) Beta 9H collected at a surface pressure of 30mN/m, circled diffraction spot corresponds to 1/3 {422}; square: {220} (b) Beta 9H collected at a surface pressure of 40mN/m, circle indicates out of phase diffraction spots (c) Beta 9H collected at surface pressure of 50mN/m, circle indicates multiple out of phase diffraction spots (d) Beta 3 collected at a surface pressure of 30mN/m. (by Wei Su)

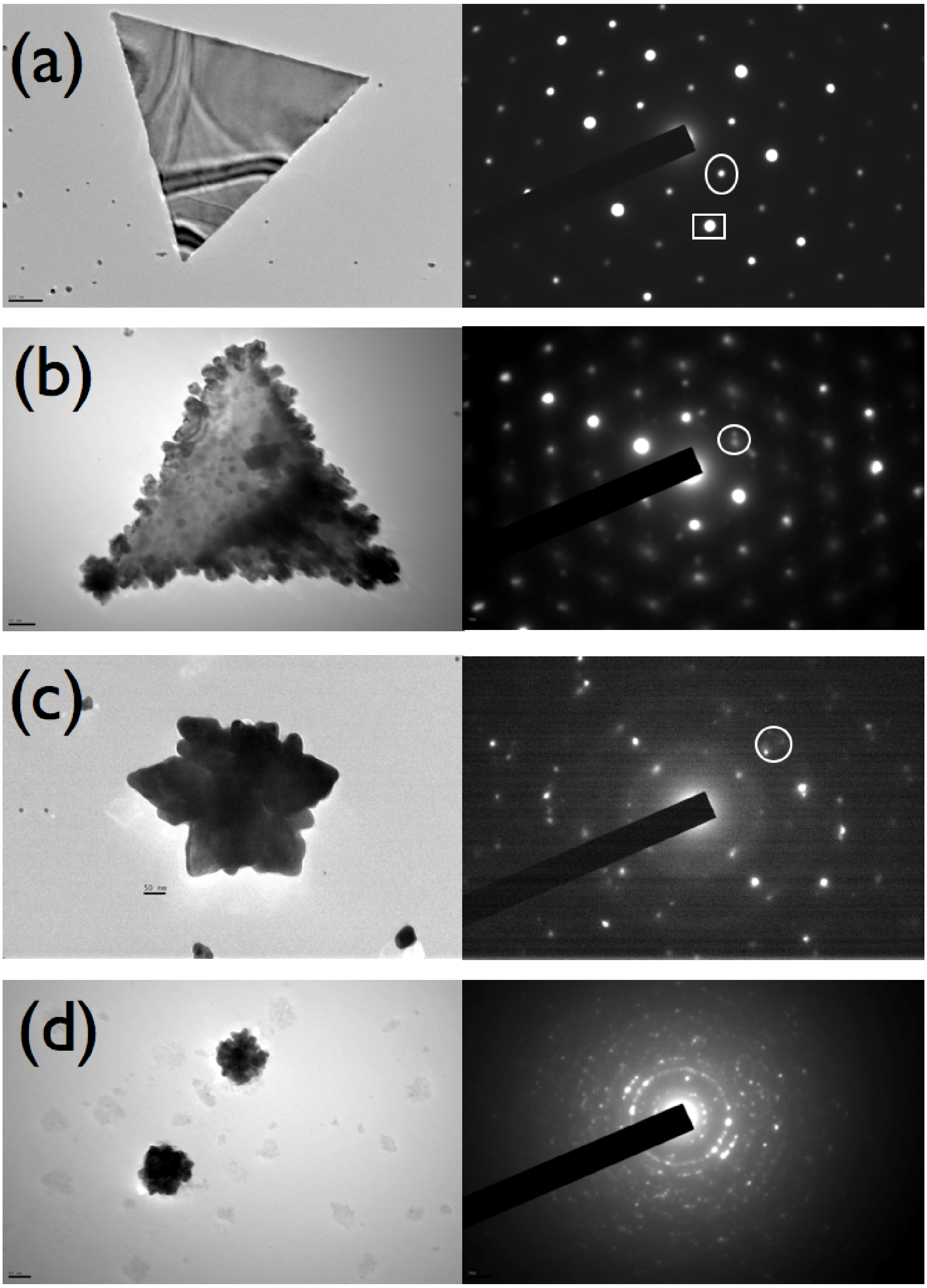

At 50mN/m, we observe through the TEM image that the structure formed is no longer a triangle, but instead a "star-like" figure 4.4. that has a diameter from point to point of approximately 460 nm. Qualitatively, at these higher pressures, these "star-like" structures appear to be formed from several overlapping triangles. The electron diffraction pattern of this structure upon close examination still has the hexagonal symmetry found in the other two gold structures. However, the multiple spots effect is more pronounced indicating that the structure is more polycrystalline in nature than the rough triangle.

We have also conducted experiments at surface pressures below 30mN/m, ranging from 5mN/m to 20mN/m. In these experiments, we also observe the formation of triangular structures similar to those formed at 30mN/m in figure 4.4, but, at surface pressures below 30mN/m, the yield of triangles is lower due to the lower number of peptide aggregates present between the pressures of 5-20 mN/m. Since the amount of peptide at the interface is the same at all surface pressures, we hypothesize that an aggregate of a critical size is necessary for the formation of the single crystal triangle. This phenomena also explains why at higher surface pressures, as is the case for 40mN/m and 50mN/m, the electron diffraction and TEM images indicate the presence of multiple single crystals since the peptide aggregates are much closer together at these higher surface pressures.

Figure 4.5 TEM images of triangular nanoplatelets and related structures: (a) triangle and hexagon (b) truncated triangle (c) truncated triangle exhibiting further growth (d) saw tooth structure (done by Wei Su)

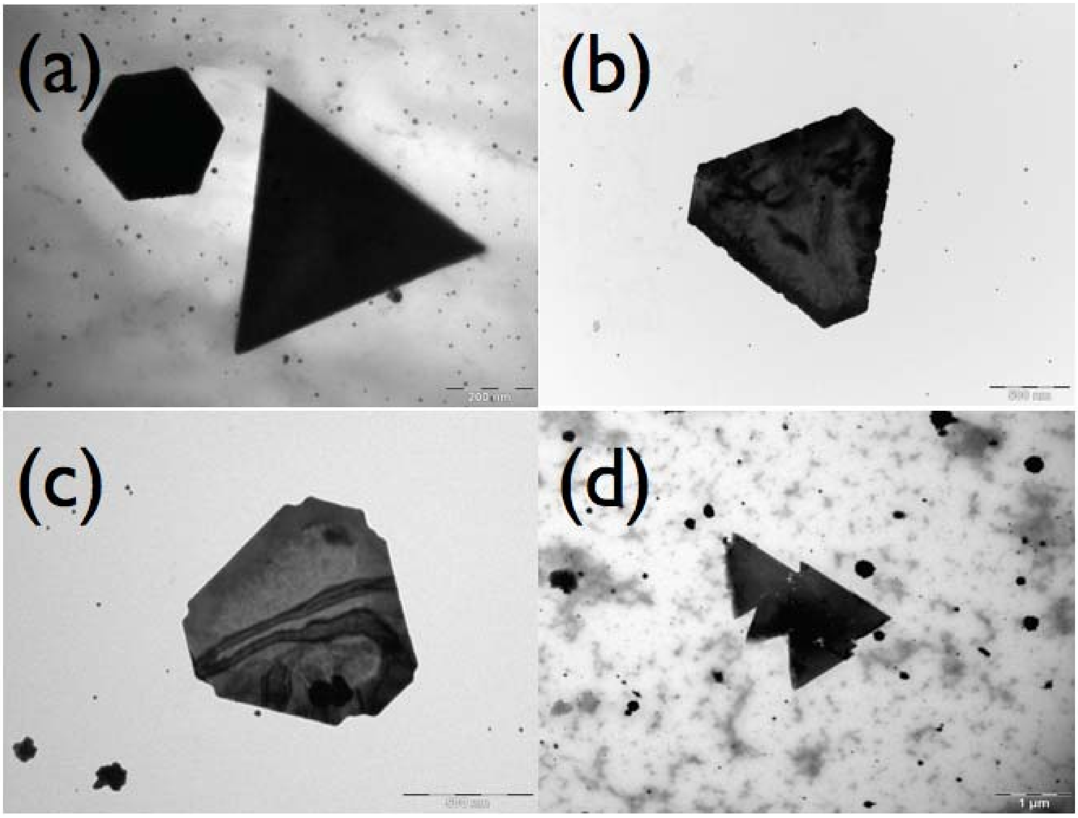

The proximity of the peptides changes between 80 Å^2/molecule (Π=30 mN/m) and 65 Å^2/molecule (Π=50 mN/m) as can be seen in figure 4.2. As the peptide film is compressed the peptides no longer have space to arrange themselves in their preferred orientation at the interface causing them to rearrange. Similar phenomena has been observed upon compression of calcium carbonate templating molecules in which an increase in surface pressure caused the molecules to tilt[119] in one case exposing a different functional group to the interface[100]. We believe that this change in proximity of neighbouring peptides causes imidazole groups in the histidine residues of the peptides to no longer always be parallel to the air/water interface leading to multiple single crystals being formed out of phase at the higher surface pressures. Numerous samples obtained from these experiments also show structures related to triangles such as hexagons, truncated triangles, and saw tooth structures. Images of these structures can be seen in figure 4.5. The hexagons and truncated triangles are found in samples obtained from surface pressures of 30mN/m and lower. The size of these structures indicates that the hexagon forms first and, subsequently, growth on three sides of the hexagon are suppressed to form a truncated triangle, and, finally, an equilateral triangle. At pressures larger than 30 mN/m, the saw tooth structure forms and appears to be a series of triangles connected along their vertices. We again hypothesize that this is a result of the proximity of peptide aggregates at higher pressures.

Figure 4.6 AFM images obtained for a truncated triangle at a surface pressure of 30mN/m (a) Three dimensional image (b) cross section and corresponding thickness profile. (by Lorraine Leon and Wei Su)

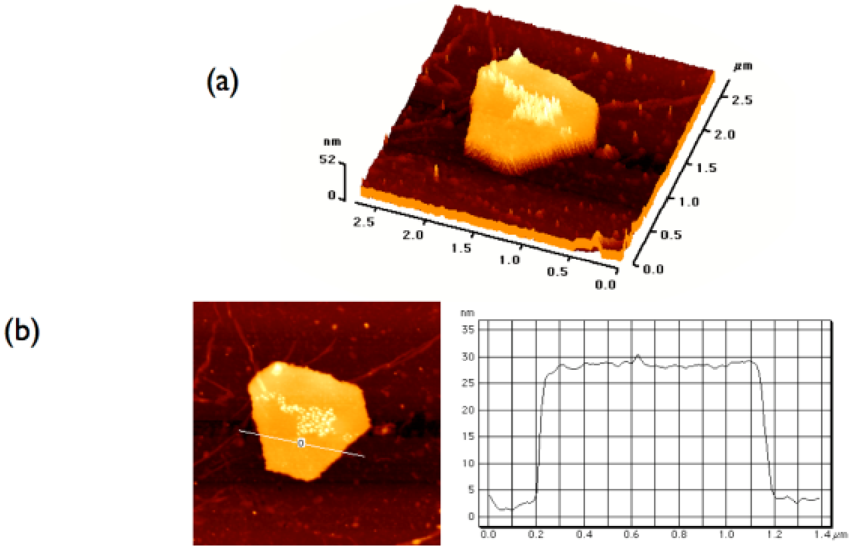

In order to try to understand the formation of these triangular and related structures, two additional experiments are conducted. First, Atomic Force Microscopy (AFM) is applied to determine the thickness of these structures. The AFM measurements are shown in figure 4.6. They indicate that the truncated triangle has a thickness of approximately 20 nm. Therefore, the structures we have been observing are confirmed to platelet structures and not pyramidal. The thinness of these structures is also confirmed using electron diffraction with tilting. In figure 4.4a, the diffraction pattern corresponding to the triangle formed at 30mN/m shows the forbidden 1/3 {422} reflection. This reflection is only seen in platelet structures in which the surface of the gold is flat[107, 118, 120, 121].

Second, a control experiment is conducted at 30mN/m using the Beta 3 peptide that contains no histidine. The TEM images and diffraction patterns for these experiments are shown in figure 4.4d. Clearly, gold was reduced at the interface. However, the formation of triangular platelets and related structures did not occur. Instead, we observe circular particles with diameters of approximately 100 nm and no preferential growth of any particular plane of gold. This control experiment clearly indicates that the reduction of gold in our system is attributed to the tryptophan residue in both sequences, but that the histidine residue is responsible for providing a directionality of growth and the formation of triangular platelets with the {111} face parallel to the air/water interface. Many metals have facets dominated by the {111} facet, indicating a low energy plane [123]. We suggest that the mechanism of growth of these triangular particles relies on the imidazole side chain binding to the {111} face of gold and thus inhibiting the growth of that particular plane or, in other words, acting as a capping agent. These fast growing facets will eventually disappear during growth, resulting in a crystal dominated by the slow growing facets[122]. This phenomena of imidazole capping the {111} facet has been observed previously in other imidazole containing molecules such as ionic liquids [120] and C18-

imidazole surfactants[123]. In the case of the ionic liquid study, higher concentrations produce plate-like particles similar to those observed at our interfaces, while low concentrations produce polyhedron like particles. This indicated that at lower concentrations, the amount of imidazole containing molecules is not sufficient to inhibit growth of other crystal planes [120].

4.4 Conclusion

We have demonstrated that the smooth single crystal triangular gold nanoplatelets could be formed by using rationally designed peptide Beta 9H optimally at surface pressure of 30mN/m without the use of extra reducing agents or high temperatures. The rational design has incorporated a tryptophan residue that isresponsible for the reduction of Au^{3+} to Au^0 and histidine residues that inhibit the growth of the {111} facet of gold. In addition, we have shown that by increasing the surface pressure of the Beta 9H peptide film, we promote more complex structures as a function of surface pressure, resulting in a mosaic of structures such as rough triangular platelets, saw tooth structures, and “star-like” structures that, in contrast to low surface pressure structures, are polycrystalline.

The characterization of crystallization using rationally designed peptides confined to interfaces has allowed us to access biomimetic pathways that lead to complexity in metallic nanostructure. These biologically inspired materials synthesis processes illustrate the relationship between a dynamic supramolecular template and the final crystalline product. The formation of single crystalline triangular platelets at low surface pressures and polycrystalline multi-faceted structures at higher pressures suggests a mechanism for growth of the crystalline phase that is more complex than direct epitaxy. Each surface pressure results in a unique set of growth conditions for the final inorganic structure, indicating that the phase behaviour of the peptide and the dynamics of self-assembly play a critical role in determining the final structure of the composite material.

References

1. P. Alivisatos, *Science,* 1996, 271, 933-937.
2. J. Zhag, R. E. Campbell, A. Y. Ting and R. Y. Tsien, *Nature Rev. Mol. Cell Biol.,* 2002, 3 , 906.
3. M. Achermann, M. A. Petruska, S. Kos, D. L. Smith, D. D. Koleske and V. I. Klimov, *Nature,* 2004, 429, 642.
4. S. Lu and A. Madhukar, *Nano Lett.,* 2007, 7, 3443.
5. L. Medintz, H. T.Uyeda, E. R. Goldman and H. Mattoussi, *Nature Materials* 2005, 4, 435-446.
6. S. A. Ivanov, A. Piryatinski, J. Nanda, S. Tretiak, K. R. Zavadil, W. O. Wallace, D. Werder and V. I. Klimov, J. *Am. Chem. Soc.*,2007, 129, 38, 11708-11719.
7. F. Xu, V. Volkov, Y. Zhu, H. Bai, A. Rea, N. V. Valappil, W. Su, X. Gao, I. L. Kuskovsky and H. Matsui, *J. Phys. Chem. C,* 2009, 113, 45.
8. S. Kim, B. Fisher, H. J. Eisier and M. Bawendi, *J. Am. Chem. Soc.,* 2003, 125, 11466.
9. J. R. Lakowicz, *Principles of Fluorescence Spectroscopy*, Plenum Publishing Corporation, 2nd edition (July 1, 1999)
10. S. A. Crooker, J. A. Hollingsworth, S. Tretiak and V. I. Klimov, *Phys. ReV. Lett.,* 2002, 89, 186802.
11. J. R. Lakowicz, *Principles of Fluorescence of Spectroscopy,* 2nd ed., Kluwer Academic/Plenum: New York, 1999, 368.

12. L. Medintz, L. Berti, T. Pons, A. F. Grimes, D. S English, A. Alessandrini, P. Facci and H. Mattoussi, *Nano Lett.,* 2007, 7, 1741.
13. Sukhanova, J. Devy, L. Venteo, H. Kaplan, M.Artemyev, V. Oleinikov, D. Klinov, M. Pluot, J. H. M. Cohen and I. Nabiev, *Anal. Biochem.,* 2004, 324, 60.
14. X. Wu, H. Liu, J. Liu, K. N. Haley, J. A. Treadway, J. P. Ge, N. Larson, F. Peale and M. P. Bruchez, *Nat. Biotechnol.*, 2003, 21, 41.
15. R. Wargnier, A. V. Baranov, V. G. Maslov, V. Stsiapura, M. Artemyev, M. Pluot, A. Sukhanova and I. Nabiev, *Nano Lett.,* 2004, 4, 3.
16. Wang, C. Chen, C. Wei, Y. Chen, C. Lai, M. Ho and P. Chou, *J. Phys. Chem. C*, 2009,113, 15548-15552.
17. H. Wang, C. W. Chen, Y. T. Chen, C. M. Wei, Y. F. Chen, C. W. Lai, M. L. Ho, P. T. Chou and M. Hofmann, *Appl. Phys. Lett,*. 2010, 96, 071906.
18. B. Murray, D. J. Norris and M. G. Bawendi, *J. Am. Chem. Soc.* 1993, 115, 19, 8706-8715.
19. R. C. Somers, M. G. Bawendi and D. G. Nocera, *Chem. Soc. Rev.,* 2007, 36, 579-591.
20. M. A. Hines and P. G.Sionnest, *J. Phys. Chem.*, 1996, 100, 468-471.
21. L. Jin, S. Li, B. Kwon and Y. Cho, *J. Appl. Phys.*, 2011, 109, 124310.
22. H. Weller, *Angew. Chem.*, 1993, 32, 41.; *Angew. Chem. Int. Ed. Engl.*, 1993, 32, 41.; *AdV. Mater.,* 1993, 5, 88.
23. M. Noh, T. Kim, H. Lee, C. K. Kim, S. Joo and K. W. Lee, *Colloids and Surfaces A: Physicochem. Eng. Aspects,* 2010, 359, 39.
24. Y. Zhang, L. Mi, P. N. Wang, J. Mab and J. Y. Chen, *Journal of Luminescence,*

2008, 128, 1948.

25. C. M. Niemeyer *Angew. Chem. Int. Edn.,* 2003, 42, 5796.
26. H. Y. Zhao, E. P. Douglas, B. S. Harrison and K. S. Schanze, *Langmuir,* 2001, 17, 8428.
27. A. Henglein, *Chem. Rev.,* 1989, 89, 1861.
28. S. P. Mondal, K. Das, A. Dhar and S. K. Ray, *Nanotechnology,* 2007, 18, 095606.
29. X. C. Wu, Y. R. Tao *J. Cryst. Growth,* 2002, 242, 3-4, 309.
30. Y. Zhou, M. Kogiso, C. He, Y. Shimizu, N. Koshizaki and T. Shimizu *Adv. Mater.,* 2007, 19, 1055.
31. J. S. Jang, U. A. Joshi and J. S. Lee *J. Phys. Chem. C,* 2007, 111, 35, 13280.
32. L. Yang, R. Xing, Q. Shen, K. Jiang, F. Ye, J. Wang and Q. Ren *J. Phys. Chem. B,* 2006, 110, 21, 10534.
33. C. Ge, M. Xu, J. Fang, J. Lei and H. Ju *J. Phys. Chem. C,* 2008, 112, 10602.
34. C. Mao, C. E. Flynn, A. Hayhurst, R. Sweeney, J. Qi, G. Georgiou, B. Iverson and A. M. Belcher PNAS, 2003, 100, 12, 6946.
35. H. Su, J. Han, Q. Dong, D. Zhang and Q. Guo *Nanotechnology,* 2008, 19, 025601.
36. X. Duan, Y. Huang, Y. Cui, J. Wang and C. M. Lieber *Nature,* 2001, 409, 66.
37. X. Wang, C. J. Summers and Z. Wang *Nano Letters*, 2004, 4, 3, 423-426.
38. H. Matsui, B. Gologan, *J. Phys. Chem. B,* 2000, 104, 3383.
39. G. J. Douberly, S. Pan, D. Walters and H. Matsui *J. Phys. Chem. B,* 2001, 105, 7612.
40. H. Matsui, R. MacCuspie, *Nano Lett.,* 2001, 1, 671.
41. R. Djalali, Y. f. Chen and H. Matsui *J. Am. Chem. Soc.*, 2002, 124, 13660.

42. M. Kogiso, S. Ohnishi, K. Yase, M. Masuda and T. Shimizu, *Langmuir*, 1998, 14, 4978.

43. International Centre for D iffraction Data (ICDD).

44. L. Spanhel, M. Haase, H. Weller and A. Henglein, *J. Am. Chem. Soc.*, 1987, 109, 5649.

45. T. Gao, T. Wang, *J. Phys. Chem. B*, 2004, 108, 20, 045.

46. T. H. Maiman, *Nature*, 1960,187(4736):493.

47. H. Yokoyama, K. Ujihara (1995) Spontaneous emission and laser oscillation in microcavities. CRC, Boca Raton, FL.

48. R. K. Chang, A. J. Campillo, (1996) Optical processes in micro-cavities. World Scientific, Singapore.

49. K. J. Vahala, *Nature*, 2003, 424, 839-846.

50. T. M. Benson, S. V. Boriskina, P. Sewell, A. Vukovic, S. C. Greedy, A. I. Nosich, (2006) Micro-optical resonators for microlasers and integrated optoelectronics. Frontiers in planar lightwave circuit technology, vol 216. Springer, Berlin, pp 39-70.

51. M. Lipson, T. Chen, K. Chen, X. Duan and L. C. Kimerling *Mat. Sci. Eng. B*, 2001, 81, 36-39.

52. H. J. Kimble, *Nature*, 2008, 453,1023.

53. J. M. Gerard, D. Barrier, J. Y. Marzin, R. Kuszelewicz, L. Manin, E. Costard, V. Thierry-Mieg and T. Rivera, *Appl .Phys. Lett*,. 1996, 69, 449.

54. M. A. Reed, J. N. Randall, R. J. Aggarwal, R. J. Matyi, T. M. Moore and A. E. Wetsel, *Phys. Rev. Lett.*, 1988, 60, 6, 535–537.

55. C. A. Leatherdale, W. K. Woo, F. V. Mikulec and M. G. Bawendi, *J. Phys. Chem. B,* 2002, 106, 7619.

56. C. Murray, C. Kagan and M. Bawendi, *Annu. Rev. Mater. Sci.,* 2000, 30, 546.

57. W. U. Huynh, J. J. Dittmer and A. P. Alivisatos, *Science,* 2002, 295, 2425.

58. V. I. Klimov, A. A. Mikhailovsky, S. Xu, A. Malko, J. A. Hollingsworth, C. A. Leatherdale, H. J. Eisler and M. G. Bawendi, *Science,* 2000, 290, 314.

59. M. Kazes, D. Y. Lewis, Y. Ebenstein, T. Mokari and U. Banin, *Adv.Mater.,* 2002, 14, 317.

60. V. Malko, A. A. Mikhailovsky, M. A. Petruska, J. A. Hollingsworth, H. Htoon, M. G. Bawendi and V. I. Klimov, *Appl. Phys. Lett.,* 2002, 81, 1303.

61. J. Lee, V. C. Sundar, J. R. Heine, M. G. Bawendi and K. F. Jensen, *Adv.Mater.*, 2000, 12, 1102.

62. M. V. Artemyev and U. Woggon, *Appl. Phys. Lett.,* 2000, 76, 1353.

63. X. Fan, M. C. Lonergan,Y. Zhang and H.Wang, *Phys. Rev. B,* 2001, 64, 115310.

64. C. E. Finlayson, D. S. Ginger and N. C. Greenham, *Chem. Phys. Lett.,* 2001, 338, 83.

65. C. E. Finlayson, D. S. Ginger and N. C. Greenham, *Appl. Phys. Lett.,* 2000, 77, 2500.

66. S. V. Gaponenko, V. N. Bogomolov, E. P. Petrov, A. M. Kapitonov, D. A. Yarotsky, I. I. Kalosha, A. A. Eychmueller, A. L. Rogach, J. McGilp, U. Woggon and F. Gindele, J. *Lightwave Technol.,* 1999, 17, 2128.

67. Y. A. Vlasov, N. Yao and D. J. Norris, *Adv. Mater.*, 1999, 11, 165.

68. Y. A. Vlasov, K. Luterova, I. Pelant, B. Honerlage, and V. N. Astratov, *Thin Solid Films,* 1999, 318, 93.

69. M. Purcell, *Phys. Rev.,* 1946, 69, 11-12, 681.

70. J. M. Grard, B. Sermage, B. Gayral, B. Legrand, E. Costard and V. Thierry-Mieg, *Phys. Rev. Lett.,* 1998, 81, 5, 1110-1113.

71. J. P. Reithmaier, G. Sek, A. Loffler, C. Hofmann, S. Kuhn, S. Reitzenstein, L.V. Keldysh, V.D. Kulakovskii, T.L. Rei-necke and A. Forchel, *Nature,* 2004, 432, 7014,197-200.

72. S. A. Ivanov, A. Piryatinski, J. Nanda, S. Tretiak, K. R. Zavadil, W. O. Wallace, D. Werder and V. I. Klimov, *J. Am. Chem. Soc.,* 2007, 129, 38, 11708-11719.

73. C. B. Murray, D. J. Norris and M. G. Bawendi, *J. Am. Chem. Soc.,* 1993, 115, 19, 8706-8715.

74. R. C. Somers, M. G. Bawendi and D. G. Nocera, *Chem. Soc. Rev.,* 2007, 36, 579-591.

75. M. A. Hines and P. G.Sionnest, *J. Phys. Chem.,* 1996, 100, 468-471.

76. D. L Smith, in "Plasma technology in Manufacturing of VLSI" (ed. Braun D. and Ainsprooc N.) Mir, Moscow, 1987, 245-264.

77. J. R. Hollahan, A.T. Bell eds. "Techniques and Applications of Plasma Chemistry", John Wiley, New York 1974.

78. W. Sark, P. Frederix, D. Heuvel, H. C. Gerritsen, A. A. Bol, J. Lingen, C. Donega and A. Meijerink, *J. Phys. Chem. B,* 2001, 105, 35.

79. M. V. Artemyev and U. Woggon, *Appl. Phys. Lett.,* 2000, 76, 11, 1353-1355.

80. S. Mann, *Nature*, 1993, 365, 499-505.

81. C. Zaremba, A. Belcher, M. Fritz, Y. Li, S. Mann, P. Hansma, D. Morse, J. Speck and G. Stucky, *Chem. Mater*, 1996, 8, 679-690.

82. S. Weiner and H. Wagner, *Annual Reviews in Materials Science*, 1998, 28, 271-298.

83. E. Bäuerlein, *Angew. Chem. Int. Ed.*, 2003, 42, 614-641.

84. E. Katz and I. Willner, *Angew. Chem. Int. Ed.*, 2004, 43, 6042-6108.

85. S. Eustis and M. El-Sayed, *Chem. Soc. Rev.*, 2006, 35, 209-217.

86. F. Meldrum and H. Cölfen, *Chemical Reviews*, 2008, 108, 4332-4432.

87. M. Daniel and D. Astruc, *Chem. Rev*, 2004, 104, 293-346.

88. C. Johnson, E. Dujardin, S. Davis, C. Murphy and S. Mann, *J. Mater. Chem.*, 2002, 12, 1765-1770.

89. M. Grzelczak, J. Pérez-Juste, P. Mulvaney and L. Liz-Marzan, *Chemical Society Reviews*, 2008, 37, 1783-1791.

90. Y. Sun and Y. Xia, *Science*, 2002, 298, 2176.

91. L. Wang, X. Chen, J. Zhan, Y. Chai, C. Yang, L. Xu, W. Zhuang and B. Jing, *J. Phys. Chem. B*, 2005, 109, 3189-3194.

92. C. Nehl, H. Liao and J. Hafner, *Nano Lett*, 2006, 6, 683-688.

93. N. Rosi and C. Mirkin, *Chem. Rev*, 2005, 105, 1547-1562.

94. M. Dickerson, K. Sandhage and R. Naik, *Chemical Reviews*, 2008, 108, 4935-4978.

95. L. Polavarapu and Q. Xu, *Nanotechnology*, 2008, 19, 075601.

96. C. Chen, P. Zhang and N. Rosi, *J. Am. Chem. Soc*, 2008, 130, 13555-13557.

97. M. Tomczak, D. Glawe and L. Drummy, *J. Am. Chem. Soc.*, 2005, 127, 12577-12582.

98. Y. Yao, W. Dong, S. Zhu, X. Yu and D. Yan, *Langmuir*, 2009, 25, 13238-13243.

99. M. Reches and E. Gazit, *Science*, 2003, 300, 625-627.

100. S. Cavalli, D. C. Popescu, E. E. Tellers, M. R. J. Vos, B. P. Pichon, M. Overhand, H. Rapaport, N. A. J. M. Sommerdijk and A. Kros, *Angew. Chem. Int. Ed.*, 2006, 45, 739-744.

101. R. Djalali, Y. Chen and H. Matsui, *J. Am. Chem. Soc*, 2003, 125, 5873-5879.

102. M. Lamm, N. Sharma, K. Rajagopal, F. Beyer, J. Schneider and D. Pochan, *Advanced Materials*, 2008, 20, 447-451.

103. N. Sharma, A. Top, K. Kiick and D. Pochan, *Angew. Chem. Int. Ed.*, 2009, 48, 7078-7082.

104. M. Iosin, P. Baldeck and S. Astilean, *Journal of Nanoparticle Research*, 2010, 12, 2843-2849.

105. J. M. Slocik, M. O. Stone and R. R. Naik, *Small*, 2005, 1, 1048-1052.

106. R. Mitra and P. Das, *The Journal of Physical Chemistry C*, 2008, 112, 8159-8166.

107. S. Shankar, A. Rai, B. Ankamwar, A. Singh, A. Ahmad and M. Sastry, *Nature Materials*, 2004, 3, 482-488.

108. C. Hansen, F. Westerlund, K. Moth-Poulsen, R. Ravindranath, S. Valiyaveettil and T. Bjornholm, *Langmuir*, 2008, 24, 3905-3910.

109. K. Nørgaard and T. Bjørnholm, *Chemical communications*, 2005, 2005, 1812-1823.

110. N. Markovich, R. Volinsky and R. Jelinek, *J. Am. Chem. Soc.*, 2009, 131, 2430-2431.

111. P. Chou and G. Fasman, *Biochemistry*, 1974, 13, 222-245.

112. H. Xiong, B. Buckwalter, H. Shieh and M. Hecht, *Proc Natl Acad Sci US A*, 1995, 92, 6349-6353.

113. B. Glisic, S. Rajkovic, M. Zivkovic and M. Djuran, *Bioorganic Chemistry*, 2010, 38, 144-148.

114. J. Cuadrado, W. Zhang, W. Hang and V. Majidi, *Journal of Environmental Monitoring*, 2000, 2, 355-359.

115. L. Leon, P. Logrippo and R. Tu, *Biophysical Journal*, 2010, 99, 2888-2895.

116. C. Lheveder, S. Hénon, R. Mercier, G. Tissot, P. Fournet and J. Meunier, *Review of Scientific Instruments*, 1998, 69, 1446.

117. Y. Shao, Y. Jin and S. Dong, *Chemical communications*, 2004, 1104-1105.

118. Y. Sun, B. Mayers and Y. Xia, *Nano Letters*, 2003, 3, 675-679.

119. E. DiMasi, S. Y. Kwak, B. P. Pichon and N. A. J. M. Sommerdijk, *CrystEngComm*, 2007, 9, 1192-1204.

120. J. Zhu, Y. Shen, A. Xie, L. Qiu, Q. Zhang and S. Zhang, *J Phys Chem C*, 2007, 111, 7629-7633.

121. V. Germain, J. Li, D. Ingert, Z. Wang and M. Pileni, *J. Phys. Chem. B*, 2003, 107, 8717-8720.

122. Y. Yin and A. Alivisatos, *Nature*, 2004, 437, 664-670.

123. S. Hsu, K. Hsu, M. Leong and I. Lin, *Dalton Transactions*, 2008, 2008, 1924-1931.

124. N. Kumar, C. Maldarelli, C. Steiner and A. Couzis, *Langmuir*, 2001, 17, 7789-7797.